

GIANT METREWAVE RADIO TELESCOPE OBSERVATIONS OF HEAD–TAIL RADIO GALAXIES

BINY SEBASTIAN, DHARAM V. LAL AND A. PRAMESH RAO

National Center for Radio Astrophysics - Tata Institute of Fundamental Research Post Box 3, Ganeshkhind P.O., Pune 41007, India;
biny@ncra.tifr.res.in

Draft version November 10, 2018

ABSTRACT

We present results from a study of seven large known head–tail radio galaxies based on observations using the Giant Metrewave Radio Telescope at 240 and 610 MHz. These observations are used to study the radio morphologies and distribution of the spectral indices across the sources. The overall morphology of the radio tails of these sources is suggestive of random motions of the optical host around the cluster potential. The presence of the multiple bends and wiggles in several head–tail sources is possibly due to the precessing radio jets. We find steepening of the spectral index along the radio tails. The prevailing equipartition magnetic field also decreases along the radio tails of these sources. These steepening trends are attributed to the synchrotron aging of plasma toward the ends of the tails. The dynamical ages of these sample sources have been estimated to be $\sim 10^8$ yr, which is a factor of six more than the age estimates from the radiative losses due to synchrotron cooling.

Subject headings: galaxies: active — galaxies: jets — galaxies: nuclei — galaxies: structure — radio continuum: galaxies

1. INTRODUCTION

It is well known that many radio galaxies have a double radio structure, with the two extended components symmetrically located with respect to the parent host galaxy. Head–tail galaxies discovered by Ryle & Windram (1968) occur in clusters of galaxies and are characterized by a head identified with the optical galaxy and two tails sweeping back from the head forming an angle with the galaxy at the apex. These sources are understood to be Fanaroff–Riley type I (Fanaroff & Riley 1974) radio sources moving through the gas in the cluster, and the shape of the source is due to the diffuse radio–emitting plasma being decelerated by the intracluster medium (ICM, Miley et al. 1972; Bliton et al. 1998). Jaffe & Perola (1973) suggested two models based on this idea: the independent blob model and the magnetospheric model. According to the independent blob model, blobs of plasma were ejected from the galaxy, and they trail behind the galaxy because of the ram pressure that acts on them. The magnetospheric model has strong magnetic fields in the galaxy that are stretched out by the supersonic motion of the galaxy. The latter model sought to explain the morphology by using the motion of relativistic electrons ejected from the galaxy’s nuclear region along these magnetic field lines. However, later ram pressure bending models were preferred over the magnetospheric model, and, subsequently, the beam models that involved the bending of continuous jets by the ram pressure replaced independent blob models (Begelman et al. 1979; Jones & Owen 1979), which is supported by several three-dimensional hydrodynamic simulations (Williams & Gull 1984; Balsara & Norman 1992; Pfrommer & Jones 2011).

Additionally, the role played by magnetic fields in the evolution and dynamics of head–tail galaxies is barely explored. Miley (1973) noticed that the polarization distributions of head–tail galaxies become more ordered and also the polarization percentage increases as one moves along the tail away from the host galaxy. This

increase in the polarization fraction was one of the reasons that prompted Jaffe & Perola (1973) to propose a magnetospheric model. The increase in polarization percentage is higher than what is expected according to synchrotron theory, due to the steepening of the spectrum, and the polarization vectors were noticed to be aligned across the tail perpendicular to the ridge line pointing toward a very ordered magnetic field that runs parallel to the tail (Feretti et al. 1998).

Recently, efforts to reproduce the observed morphology of tailed sources using three-dimensional magnetohydrodynamic simulations are being undertaken (Jones et al. 2017; Gan et al. 2017). Head–tail radio sources are also used to identify clusters and also as probes of cluster properties (Blanton et al. 2000, 2001; Blanton et al. 2003; Wing & Blanton 2011; Paterno-Mahler et al. 2016).

Pacholczyk & Scott (1976) studied the spatial variation of the spectral index, flux density, and polarization of a few head–tail galaxies. They find that head–tail radio galaxy evolves into three distinct regions. The first region, which is the closest to the core, has a brightness peak from which it starts to drop along with an increase in the spectral index. This was thought to be due to particle acceleration, expansion, and synchrotron losses that occur in this region. The second region has a roughly constant luminosity and spectral index, which was attributed to the competition between the acceleration of particles due to turbulence and the synchrotron losses. According to ram pressure bending models, a galaxy under the influence of the central cluster potential must be moving at supersonic velocities. A bow shock is expected to form at the leading edge of the optical galaxy, causing this turbulence farther downstream. Finally, the third region is where the synchrotron losses dominate, and a steady increase in the spectral index along with a decrease in flux density is observed.

Here, we present a low-frequency study of a sample of seven head–tail radio galaxies using the Giant Metrewave Radio Telescope (GMRT). The radio morphologies

TABLE 1

SOURCES. COLUMN 1: NAME AS USED IN THIS PAPER; THE NAME OF THE CLUSTER IS GIVEN BELOW IT IN PARENTHESES. COLUMN 2: REDSHIFT. COLUMN 3: RIGHT ASCENSION. COLUMN 4: DECLINATION. COLUMN 5: ANGULAR SIZE. COLUMN 6: LINEAR SCALE FOR OUR ADOPTED COSMOLOGY. COLUMN 7: DATE OF OBSERVATION. COLUMN 8: BANDWIDTH. COLUMN 9: CENTER FREQUENCY. COLUMN 10: FLUX DENSITY CALIBRATOR. COLUMN 11: PHASE CALIBRATOR. COLUMN 12: ON-SOURCE INTEGRATION TIME.

| Object | z | R.A. | Decl. | Size (θ) | Linear scale (kpc arcsec $^{-1}$) | Obs. date | $\Delta\nu$ (MHz) | $\nu_{\text{cen.}}$ (MHz) | Flux calibrators | Phase calibrators | Int. time (hr) |
|--------------------------------|-------|-------------|-------------|----------------------|---------------------------------------|-------------|----------------------|------------------------------|---------------------|----------------------|-------------------|
| (1) | (2) | (3) | (4) | (5) | (6) | (7) | (8) | (9) | (10) | (11) | (12) |
| PKS B0053–016 (Abell 119) | 0.043 | 00 56 02.91 | –01 20 04.5 | 5.0 | 0.841 | 2016 Jun 29 | 32 | 322.6/ | 3C48 | 0025–260 | 2 |
| | | | | | | 2016 Jul 05 | 32 | 608.0 | 3C48 | 0025–260 | 2.4 |
| PKS B0053–015 (Abell 119) | 0.038 | 00 56 25.70 | –01 15 46.8 | 6.0 | 0.748 | 2016 Jun 29 | 32 | 322.6/ | 3C48 | 0025–260 | 2 |
| | | | | | | 2016 Jul 05 | 32 | 608.0 | 3C48 | 0025–260 | 2.4 |
| IC 310 (Abell 426) | 0.019 | 03 16 42.77 | +41 19 29.6 | 8.5 | 0.385 | 2002 Dec 21 | 8 | 240.3/ | 3C48, | 0314+432, | 6.5 |
| | | | | | | | | 609.6 | 3C147 | 0348+338 | 6.5 |
| NGC 1265 (Abell 426) | 0.025 | 03 18 14.86 | +41 51 27.6 | 10.5 | 0.502 | 2002 Dec 20 | 8 | 240.3/ | 3C48, | 0348+338 | 6 |
| | | | | | | | | 609.6 | 3C286 | | 6 |
| GB6 B0335+096 (2A 0335+096) | 0.038 | 03 38 14.09 | +10 05 03.9 | 8.5 | 0.748 | 2009 Dec 23 | 16 | 618.3/ | 3C48 | 0521+166 | 3.5 |
| | | | | | | 2002 May 05 | 8 | 240.3 | 3C48, | 0323+055, | 1.25 |
| | | | | | | | | | 3C147 | 0025–260 | |
| IC 711 (Abell 1314) | 0.032 | 11 34 45.66 | +48 57 21.5 | 15.0 | 0.636 | 2002 Dec 23 | 8 | 240.3/ | 3C147, | 1219+484, | 6 |
| | | | | | | | | 609.6 | 3C286 | 1252+565 | 6 |
| NGC 7385 (Cul 2247+113) | 0.026 | 22 49 54.57 | +11 36 30.1 | 12.0 | 0.522 | 2002 Dec 23 | 8 | 240.3/ | 3C286, | 2232+117, | 5.5 |
| | | | | | | | | 609.6 | 3C48 | 2250+143 | 5.5 |

and spatial structure in the radio spectrum are studied in order to understand the trends discussed above. We also present the variation of equipartition parameters, including magnetic field, along the head–tail radio galaxy. In a subsequent paper, we will discuss the total intensity and brightness gradient, the X-ray properties of these head–tail radio sources, and the morphological properties of a propagating jet as it crosses its interstellar medium (ISM) into an ICM.

This paper is organized as follows, Sections 2 and 3, respectively, describe the head–tail radio galaxy sample and GMRT observations along with data analyses. Radio images and spectral index maps of the head–tail radio galaxies, giving a brief description of the morphological and spectral features and physical parameters, are presented in Section 4. We present a discussion from our observations in light of our understanding from the literature for the sample of head–tail radio galaxies in Section 5 and summarize the salient conclusions of our study in Section 6. We define radio spectral index, α , via $S_\nu \propto \nu^\alpha$, where S_ν and ν are flux density and frequency, respectively. We adopt a cosmology with $H_0 = 69.6$ km s $^{-1}$ Mpc $^{-1}$, $\Omega_M = 0.286$, and $\Omega_\Lambda = 0.714$ (Spergel et al. 2007).

2. HEAD–TAIL GALAXY SAMPLE

Owen & Ledlow (1997) have surveyed over 500 Abell clusters of galaxies using the Very Large Array (VLA) at $\lambda = 21$ cm, and they presented radio maps of sources with complex or multiple features. They detect and list candidate head–tail radio sources in these clusters. From this list of candidate head–tail radio sources, along with the head–tail sources known in the literature, we choose only nearby, $z < 0.05$ and confirmed head–tail galaxies with an angular size of galaxy tail larger than 5 arcmin as our sample source. These 11 sources were observed with the GMRT during cycles 03 and 04 (03DVL02, 04DVL01). The data for four sources were badly affected by GMRT hardware correlator issues, so we do not include them here. Our final sample consisted of seven head–tail radio galaxies, listed in Table 1.

3. GMRT OBSERVATIONS

Our sample of seven head–tail radio galaxies was observed using the simultaneous dual–frequency (240 MHz and 610 MHz) mode of GMRT, except for two sources, where data at 240 MHz were marred by radio frequency interference (RFI) and were later observed at 325 MHz. Table 1 gives the details of the observations. The columns are as follows: (1) source name along with the name of the cluster (in parentheses); (2) redshift; (3, 4) R.A. and decl.; (5) angular size (arcmin); (6) linear scale (kpc arcsec $^{-1}$) for our adopted cosmology; (7) date of observation; (8, 9) bandwidth and center observing frequency; (10, 11) corresponding flux density and phase calibration sources; and (12) on-source integration time.

The GMRT is a low-frequency interferometer with a hybrid configuration. One-half of the antennas out of the total of 30 antennas are located within a central region of size 1.1 km, and the other half are distributed along an approximate ‘Y’ shape with a maximum baseline length of ~ 25 km. The presence of a large number of antennas in the central square, along with enhanced surface brightness at lower frequencies, makes GMRT an ideal instrument to obtain high-resolution images of the head–tail galaxies without missing much information at extended scales (Lal & Rao 2007). The angular resolution of these observations corresponds to at least 20 synthesized beams across the source, which is sufficient to provide a detailed radio morphology and allow the study of spectral structure in these sources.

3.1. Data reduction

Data sets for several target sources were flagged and calibrated using the FLAGCAL package (Prasad & Chengalur 2012), and imaged using the classic package (‘AIPS’), except for PKS B0053–016, PKS B0053–015 and GB6 B0335+0955, which were reduced using standard data-reduction procedures in classic ‘AIPS’. Flux density calibrators observed at the beginning and the end of the observations were used to calibrate the complex gains of the visibilities and correct for the bandpass shape. Phase calibration sources

observed typically once every 35 minutes were used to correct for variations in the amplitude and phase across time. Spectral channels affected by RFI were flagged, and the calibrated data were averaged in frequency using AIPS task ‘SPLAT’ before imaging to reduce the data volume. Care was taken to avoid bandwidth smearing.

The wide field of view was divided into a number of overlapping facets for imaging. After three to four rounds of phase-only self-calibration, with typical solution interval timescales of 2 minutes for self-calibration, a final amplitude and phase self-calibration were done. These sets of facets were interpolated to a single image using AIPS task ‘FLATN’ centered on the pointing position and were corrected for the primary beam using the AIPS task ‘PBCOR’. Figure 1 presents high-resolution, high-sensitivity radio images at 610 MHz (contour maps) overlaid on the SDSS *gri*-color composite images of all seven head–tail radio galaxies (see Table 1). To enhance the detailed source structure with a reasonably good sensitivity, both high and low angular resolution images at both 240/325 MHz and 610 MHz frequencies were constructed. The default high-angular-resolution images were made with $\sim 5''$ and $\sim 10''$ synthesized beams, and the low-angular-resolution images were made by tapering the visibility data at 15 k λ and restored using either a $15''$ or a $20''$ synthesized beam. The misalignment between the matched resolution images at the two frequencies, if any, was corrected, and the spectral index maps were constructed using the AIPS task ‘COMB’. We blanked pixels where the total intensity level was less than three times the rms noise level (see also Sec. 4.1) at a given frequency band in order to make spectral index maps.

4. RESULTS

4.1. Radio morphology

The radio maps of our head–tail sample radio galaxies at frequencies 610 MHz and 240/325 MHz are shown in Figures 2–8 with angular resolutions of $\sim 5''$ and $\sim 10''$, respectively. The maps are ordered in R.A. Similar to earlier published radio continuum images of X-shaped and FR II radio galaxies (e.g., Lal & Rao 2005, 2007; Lal, Hardcastle & Kraft 2008, etc.) the dynamic ranges in the maps are 900–5000 and the local noise in the vicinity of our targets are occasionally higher than the noise in empty regions. The contour levels shown in these figures are based on the rms noise in the vicinity of our targets, which is generally more, with the first contour level being 3–5 times this rms noise level. The upper panel shows the default high-resolution images, while the lower panel shows the low-resolution images. The integrated flux densities of all the sources along with previous measurements from the literature are plotted in Figure 9. Our estimates at both frequencies, 240/325 MHz and 610 MHz, agree well with other measurements. A brief description of the radio morphologies at these observing frequencies and angular resolutions of our sample sources is discussed below.

4.1.1. PKS B0053–016

Feretti et al. (1998) and O’Dea & Owen (1985) have studied PKS B0053–016 and PKS 0053–015 high-frequency using VLA. Also from their polarization studies, Mack et al. (1993) find magnetic field components

aligned with the tail. These two galaxies are members of the ACO 119 cluster. Figure 1 suggests that the host galaxy of PKS 0053–015 is moving toward the direction of the cluster center, with two very symmetric tails trailing behind. The overall motion of the galaxy follows a straight line without much evidence for a curved trajectory around the cluster center.

The radio morphology is quite symmetric and has an overall angular extent of $6'$, and the core is not very prominent. The high-resolution contour map (Figure 2) at 610 MHz resolves the jets that are ejected from the core, as two distinct radio jets. Slightly away from the core the intensity increases and the jet widens. radio galaxies. Both the jets also seem to follow a helical trajectory, and the tails seem to show symmetric wiggles. This substantiates the speculation that this has something to do with the origin of the jets, and is not due to any interaction with the ambient medium or instabilities (Kharb, Lister & Cooper 2010). This helicity is presumably introduced by the precession of the jets.

4.1.2. PKS B0053–015

Figure 1 shows that the host galaxy is not at the leading edge of the tails, unlike most head–tail galaxies. The jets are clearly ejected at wide angles. The peculiar morphology might be a consequence of the fact that one of the jets is not ejected at right angles but instead at a smaller angle with the direction of motion of the galaxy. This might also result from projection effects or an interplay of both. If the former is the reason, then the bending of the northern jet, which has a velocity component in the direction of motion, suggests that the jet experiences a very high ram pressure. The projected angular distance from the center of the cluster is only $2'.4$. It is thus possible that the galaxy is close to the cluster center, which would in turn mean higher galaxy velocity and higher ICM density and thus higher ram pressure. Galaxies in a cluster are expected to follow an orbital motion around the cluster potential well.

The radio morphology of PKS 0053–015, shown in Figure 3 is very similar to PKS B0053–016. The angular size of this head–tail galaxy is $5'.0$. The core is bright, and an increase in surface brightness as one moves slightly away from the core is seen in this galaxy as well. The jets are noticeably asymmetric. The relative distance of the flare with respect to the core is very different for both the jets. The surface brightness of the northern jet decreases at a much faster rate than that for the southern jet. Another interesting feature is the presence of wiggles along the tail. Although the jet is very asymmetric, it is worth noting that every helix, also called wiggles, seen in one jet has a counterpart in the other jet. These wiggles are very systematic and may be occurring because of the precession of the central engine.

4.1.3. IC 310

The radio morphology of IC 310, located in the Perseus cluster, is shown in Figure 4.

From an X-ray study of a few head–tail radio sources, Edge & Röttgering (1995) had predicted the presence of a BL Lac nucleus in IC 310. Later on, Aleksić et al. (2014) classified IC 310 as a high-energy peaked BL Lac, which suggests that the inclination angle of the radio jet with respect to our line of sight is small. IC 310 and

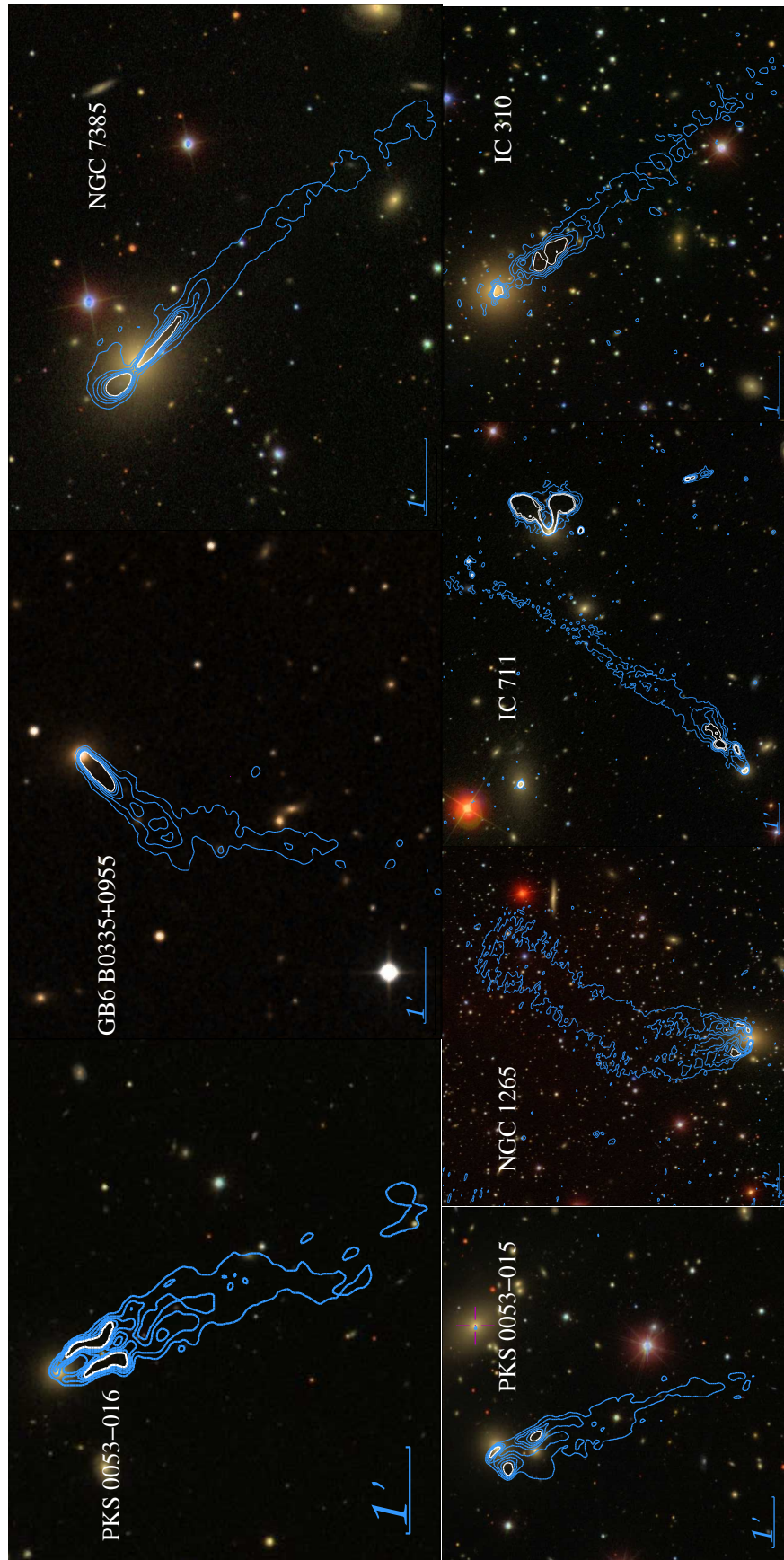


FIG. 1.— High-resolution, high sensitivity GMRT radio images (contour maps) at 610 MHz overlaid on the SDSS *gri*-color composite images of our sample sources. In clockwise order from top left, the sources are PKS 0053–016, GB6 B0335+0955, NGC 7385, IC 310, IC 711, NGC 1265 and PKS 0053–015.

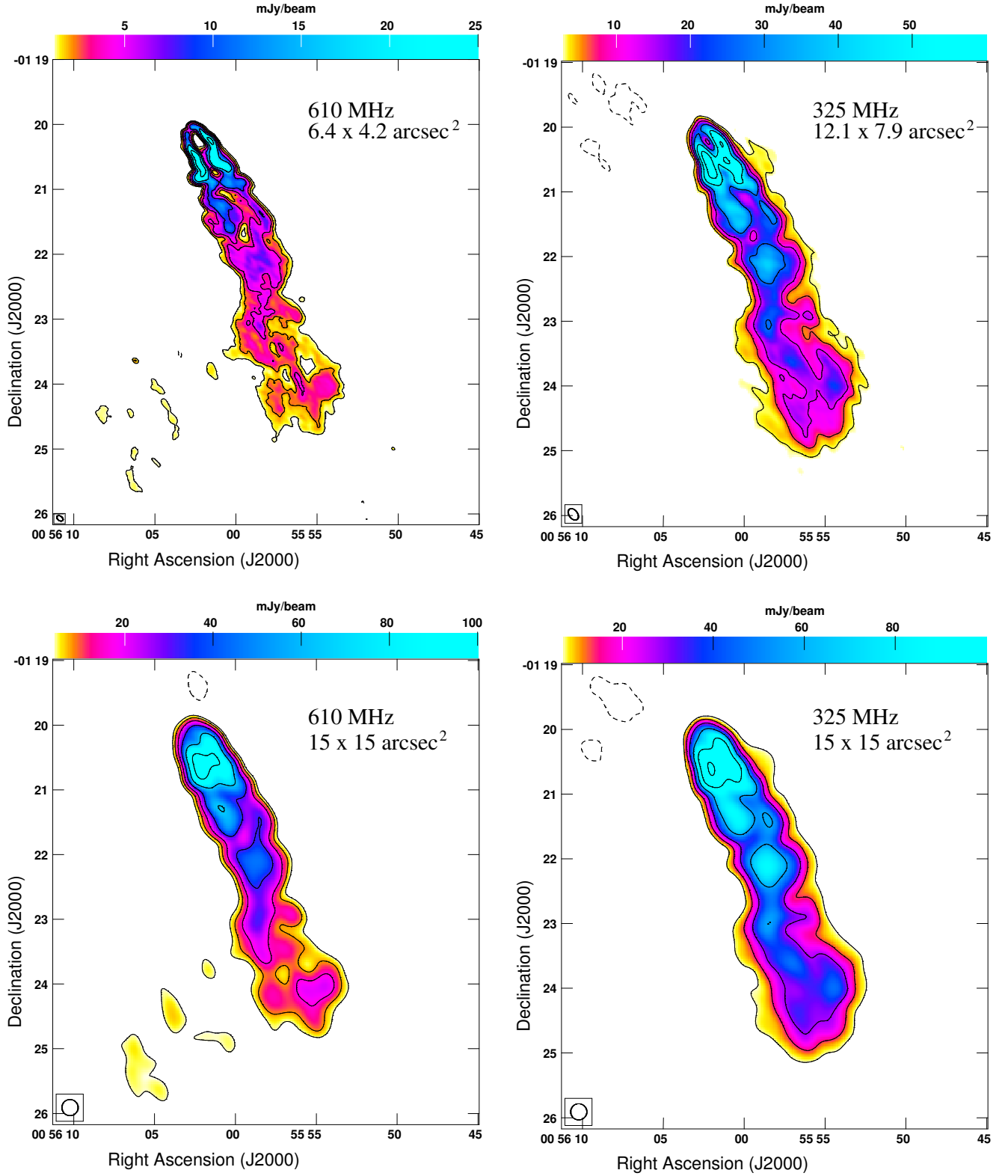


FIG. 2.— Full synthesis images of PKS B0053–016. Top left panel: image at 610 MHz with a beam size of $6''.4 \times 4''.2$ at a PA $52^\circ 1$, the peak surface brightness is $51.7 \text{ mJy beam}^{-1}$, the error bar at a source-free location is $0.3 \text{ mJy beam}^{-1}$ and the contour levels are $1.0 \times (-2, -1, 1, 2, 4, 8, 16, 32, 64, 128) \text{ mJy beam}^{-1}$. Top right panel: image at 325 MHz with a beam size of $12''.1 \times 7''.9$ at a PA $-36^\circ 7$, the peak surface brightness is $151.3 \text{ mJy beam}^{-1}$, the error bar at a source-free location is $0.8 \text{ mJy beam}^{-1}$ and the contour levels are $3.2 \times (-1, 1, 2, 4, 8, 16, 32, 64) \text{ mJy beam}^{-1}$. Bottom left panel: low-resolution image at 610 MHz with a beam size of $15'' \times 15''$, the peak surface brightness is $176.1 \text{ mJy beam}^{-1}$, the error bar at a source-free location is $1.0 \text{ mJy beam}^{-1}$ and the contour levels are $4.0 \times (-2, -1, 1, 2, 4, 8, 16, 32, 64, 128) \text{ mJy beam}^{-1}$. Bottom right panel: low-resolution image at 325 MHz with a beam size of $15'' \times 15''$, the peak surface brightness is $236.5 \text{ mJy beam}^{-1}$, the error bar at a source-free location is $2.0 \text{ mJy beam}^{-1}$ and the contour levels are $7.0 \times (-2, -1, 1, 2, 4, 8, 16, 32, 64, 128) \text{ mJy beam}^{-1}$.

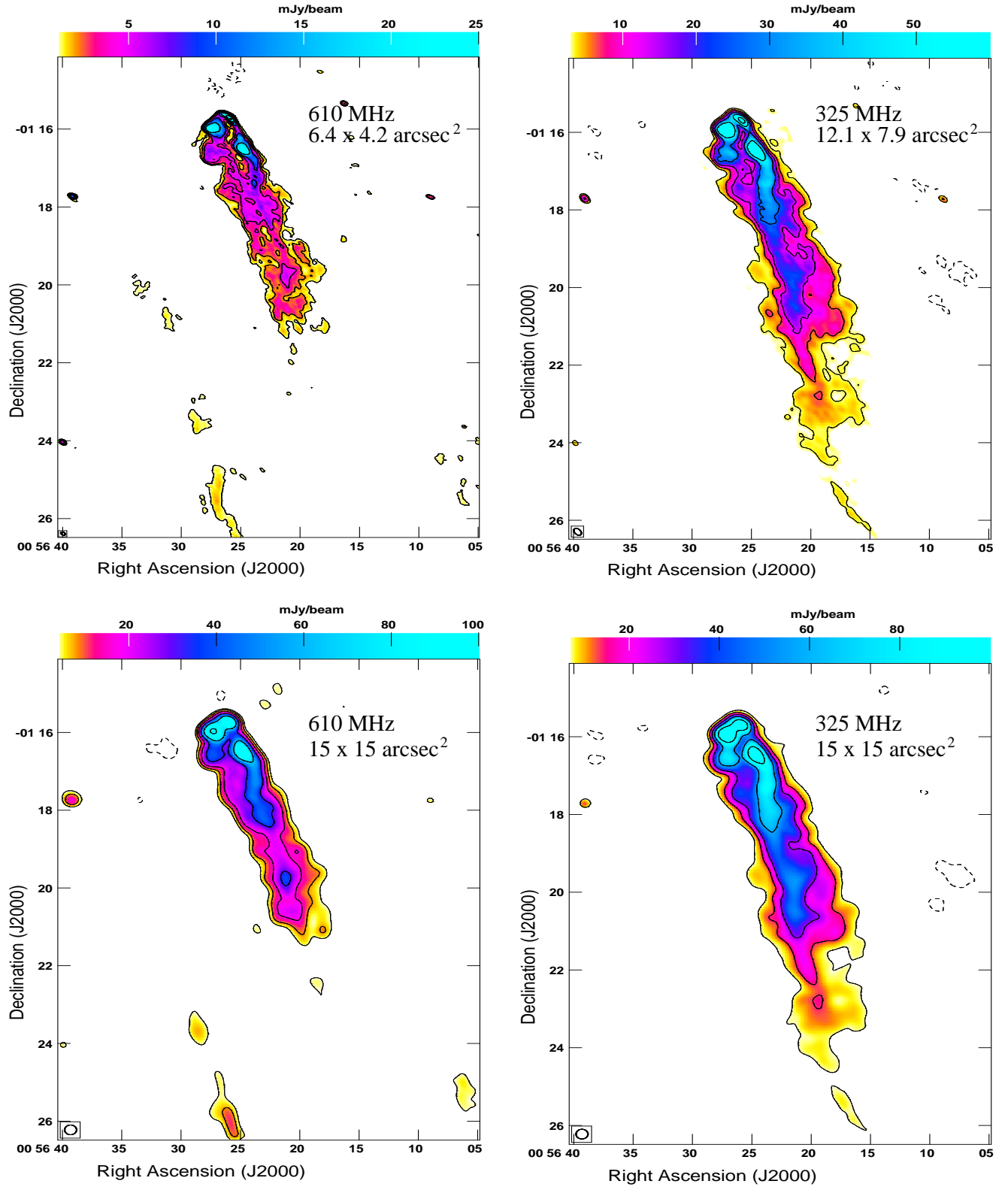


FIG. 3.— Full synthesis images of PKS B0053–015. Top left panel: image at 610 MHz with a beam size of $6''.4 \times 4''.2$ at a PA $52^\circ.1$, the peak surface brightness is $67.1 \text{ mJy beam}^{-1}$, the error bar at a source-free location is $0.3 \text{ mJy beam}^{-1}$ and the contour levels are $1.0 \times (-2, 2, 4, 8, 16, 32, 64, 128) \text{ mJy beam}^{-1}$. Top right panel: image at 325 MHz with a beam size of $12''.1 \times 7''.9$ at a PA $-36^\circ.7$, the peak surface brightness is $134.9 \text{ mJy beam}^{-1}$, the error bar at a source-free location is $0.8 \text{ mJy beam}^{-1}$ and the contour levels are $3.2 \times (-1, 1, 2, 4, 8, 16, 32, 64) \text{ mJy beam}^{-1}$. Bottom left panel: low-resolution image at 610 MHz with a beam size of $15'' \times 15''$, the peak surface brightness is $137.8 \text{ mJy beam}^{-1}$, the error bar at a source-free location is $1.0 \text{ mJy beam}^{-1}$ and the contour levels are $4.0 \times (-2, -1, 1, 2, 4, 8, 16, 32, 64, 128) \text{ mJy beam}^{-1}$. Bottom right panel: low-resolution image at 325 MHz with a beam size of $15'' \times 15''$, the peak surface brightness is $196.7 \text{ mJy beam}^{-1}$, the error bar at a source-free location is $2.0 \text{ mJy beam}^{-1}$ and the contour levels are $7.0 \times (-2, -1, 1, 2, 4, 8, 16, 32, 64, 128) \text{ mJy beam}^{-1}$.

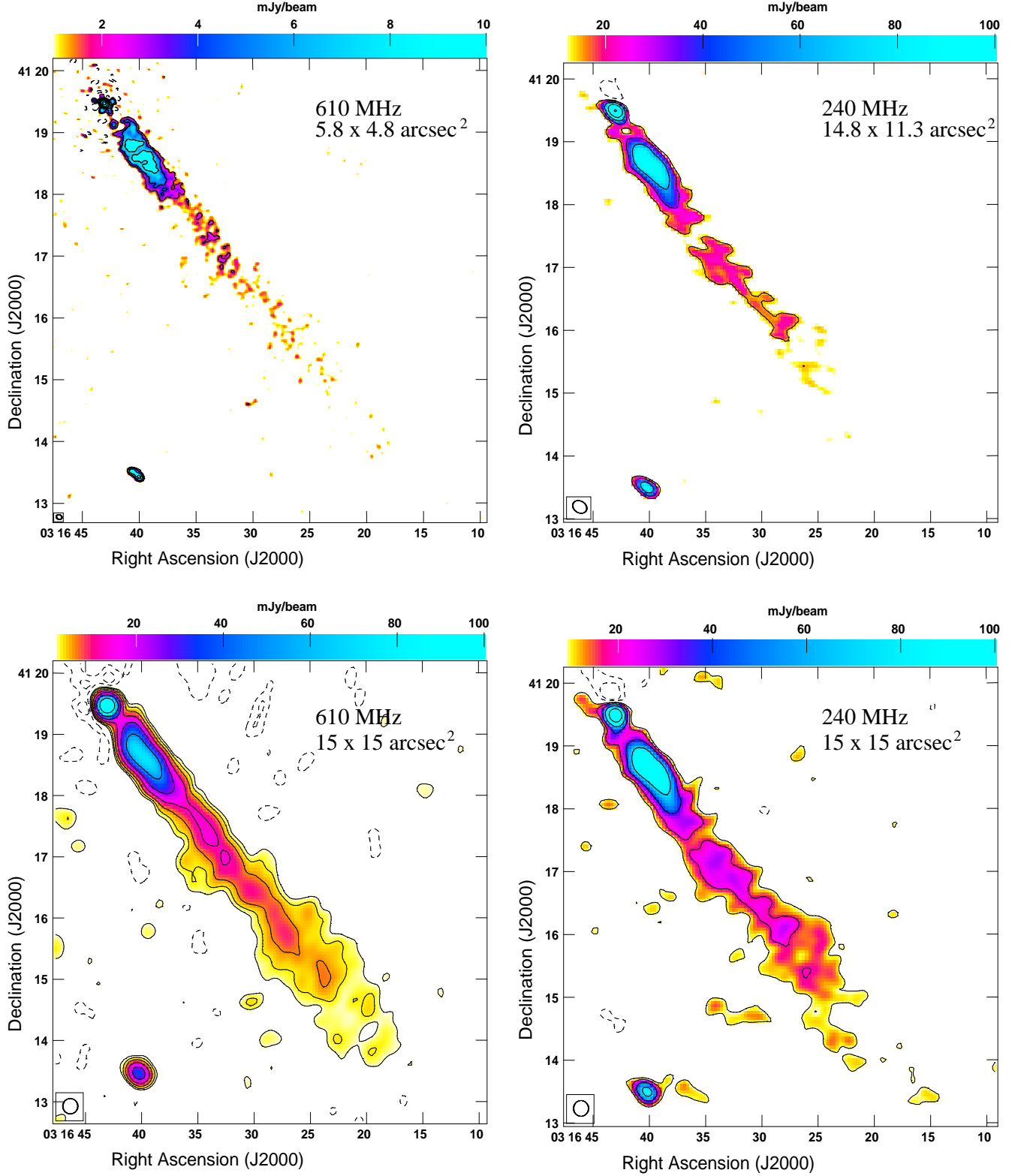


FIG. 4.— Full synthesis images of IC 310. Top left panel: image at 610 MHz with a beam size of $5''.8 \times 4''.8$ at a PA $67^\circ.8$, the peak surface brightness is $168.0 \text{ mJy beam}^{-1}$, the error bar at a source-free location is $0.3 \text{ mJy beam}^{-1}$ and the contour levels are $1.0 \times (-2, 2, 4, 8, 16, 32, 64, 128) \text{ mJy beam}^{-1}$. Top right panel: image at 240 MHz with a beam size of $14''.8 \times 11''.3$ at a PA $-62^\circ.9$, the peak surface brightness is $255.1 \text{ mJy beam}^{-1}$, the error bar at a source-free location is $3.2 \text{ mJy beam}^{-1}$ and the contour levels are $7.6 \times (-2, 2, 4, 8, 16, 32, 64) \text{ mJy beam}^{-1}$. Bottom left panel: low-resolution image at 610 MHz with a beam size of $15'' \times 15''$, the peak surface brightness is $180.5 \text{ mJy beam}^{-1}$, the error bar at a source-free location is $0.8 \text{ mJy beam}^{-1}$ and the contour levels are $1.6 \times (-2, -1, 1, 2, 4, 8, 16, 32, 64) \text{ mJy beam}^{-1}$. Bottom right panel: low-resolution image at 240 MHz with a beam size of $15'' \times 15''$, the peak surface brightness is $246.3 \text{ mJy beam}^{-1}$, the error bar at a source-free location is $3.4 \text{ mJy beam}^{-1}$ and the contour levels are $9.0 \times (-2, -1, 1, 2, 4, 8, 16, 32, 64) \text{ mJy beam}^{-1}$.

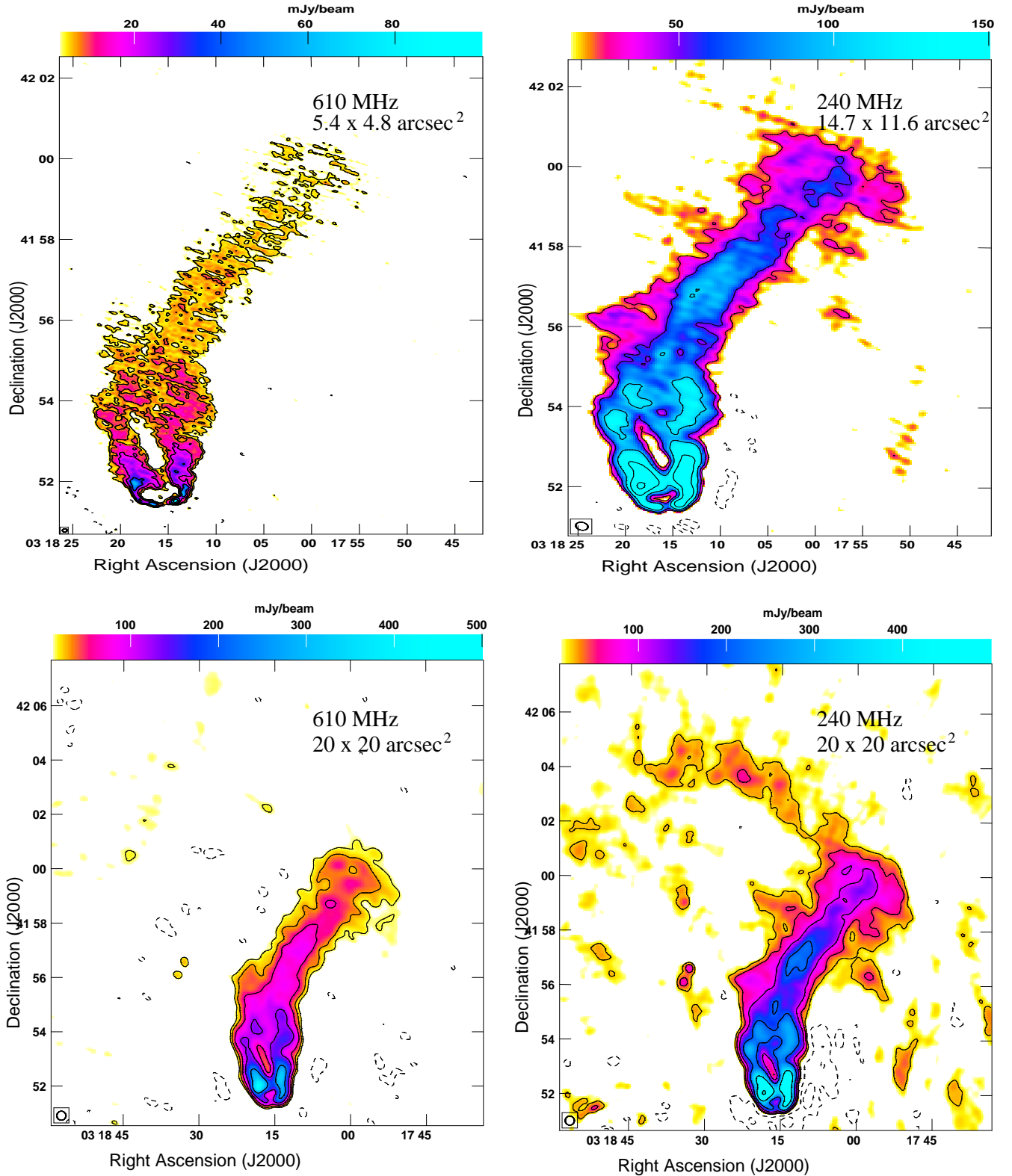


FIG. 5.— Full synthesis images of NGC 1265. Top left panel: image at 610 MHz with a beam size of $5''.4 \times 4''.8$ at a PA $-82^\circ.4$, the peak surface brightness is $100.8 \text{ mJy beam}^{-1}$, the error bar at a source-free location is $0.9 \text{ mJy beam}^{-1}$ and the contour levels are $1.0 \times (-2, 2, 4, 8, 16, 32, 64, 128) \text{ mJy beam}^{-1}$. Top right panel: image at 240 MHz with a beam size of $14''.7 \times 11''.6$ at a PA $-68^\circ.9$, the peak surface brightness is $338.3 \text{ mJy beam}^{-1}$, the error bar at a source-free location is $4.4 \text{ mJy beam}^{-1}$ and the contour levels are $13.0 \times (-2, 2, 4, 8, 16, 32, 64) \text{ mJy beam}^{-1}$. Bottom left panel: low-resolution image at 610 MHz with a beam size of $20'' \times 20''$, the peak surface brightness is $299.2 \text{ mJy beam}^{-1}$, the error bar at a source-free location is $2.6 \text{ mJy beam}^{-1}$ and the contour levels are $15.0 \times (-2, -1, 1, 2, 4, 8, 16, 32, 64, 128) \text{ mJy beam}^{-1}$. Bottom right panel: low-resolution image at 240 MHz with a beam size of $20'' \times 20''$, the peak surface brightness is $467.0 \text{ mJy beam}^{-1}$, the error bar at a source-free location is $6.4 \text{ mJy beam}^{-1}$ and the contour levels are $25.0 \times (-2, -1, 1, 2, 4, 8, 16, 32, 64, 128) \text{ mJy beam}^{-1}$.

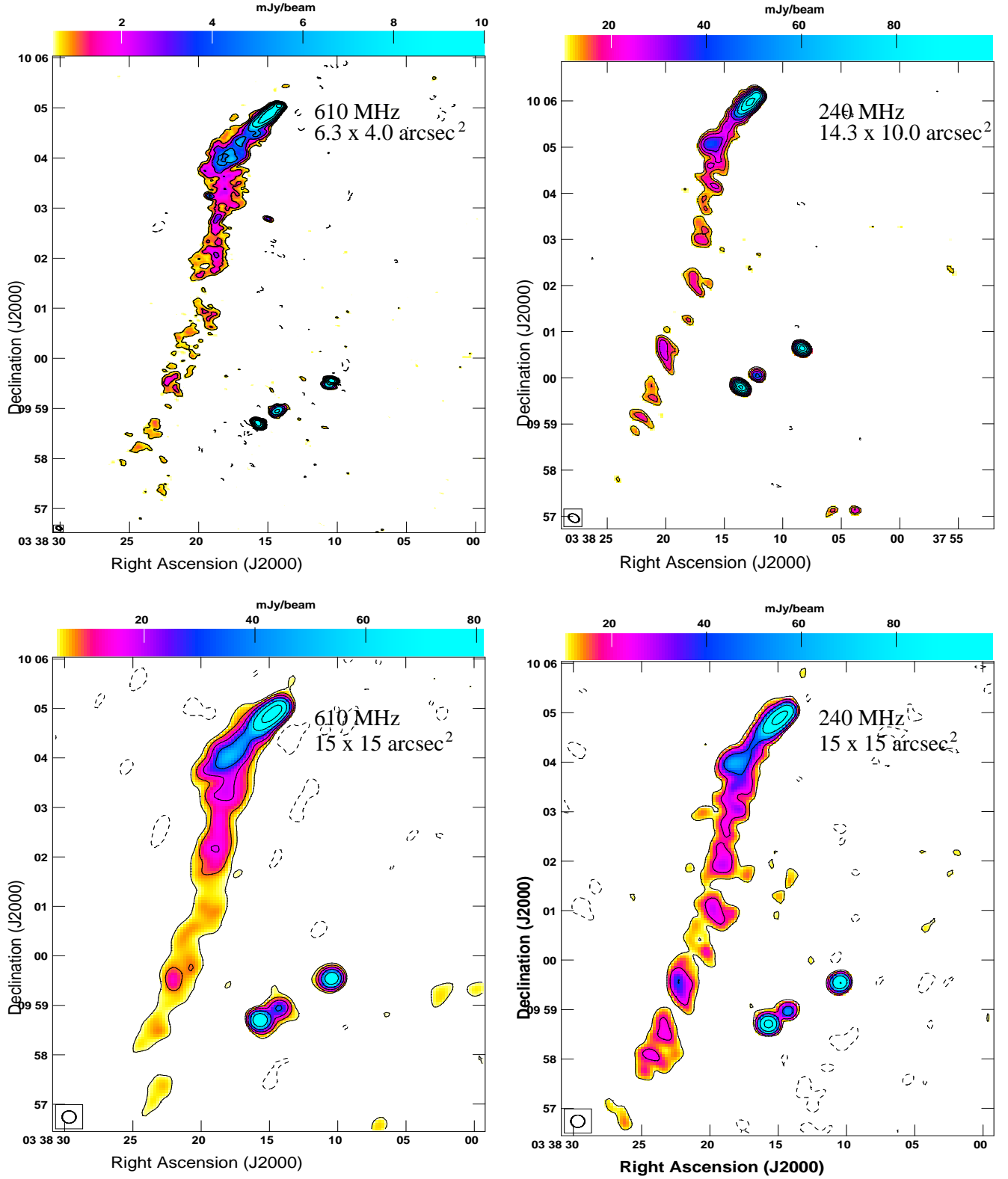


FIG. 6.— Full synthesis images of GB6 B0335+0955. Top left panel: image at 610 MHz with a beam size of $6''.3 \times 4''.0$ at a PA $69^\circ 8$, the peak surface brightness is $84.0 \text{ mJy beam}^{-1}$, the error bar at a source-free location is $0.2 \text{ mJy beam}^{-1}$ and the contour levels are $0.6 \times (-2, -1, 1, 2, 4, 8, 16, 32, 64) \text{ mJy beam}^{-1}$. Top right panel: image at 240 MHz with a beam size of $14''.3 \times 10''.0$ at a PA $59^\circ 9$, the peak surface brightness is $197.6 \text{ mJy beam}^{-1}$, the error bar at a source-free location is $2.7 \text{ mJy beam}^{-1}$ and the contour levels are $11.0 \times (-2, -1, 1, 2, 4, 8, 16)$. Bottom left panel: low-resolution image at 610 MHz with a beam size of $15'' \times 15''$, the peak surface brightness is $179.1 \text{ mJy beam}^{-1}$, the error bar at a source-free location is $1.4 \text{ mJy beam}^{-1}$ and the contour levels are $4.0 \times (-2, -1, 1, 2, 4, 8, 16, 32, 64) \text{ mJy beam}^{-1}$. Bottom right panel: low-resolution image at 240 MHz with a beam size of $15'' \times 15''$, the peak surface brightness is $210.1 \text{ mJy beam}^{-1}$, the error bar at a source-free location is $4.9 \text{ mJy beam}^{-1}$ and the contour levels are $10.0 \times (-2, -1, 1, 2, 4, 8, 16, 32, 64) \text{ mJy beam}^{-1}$.

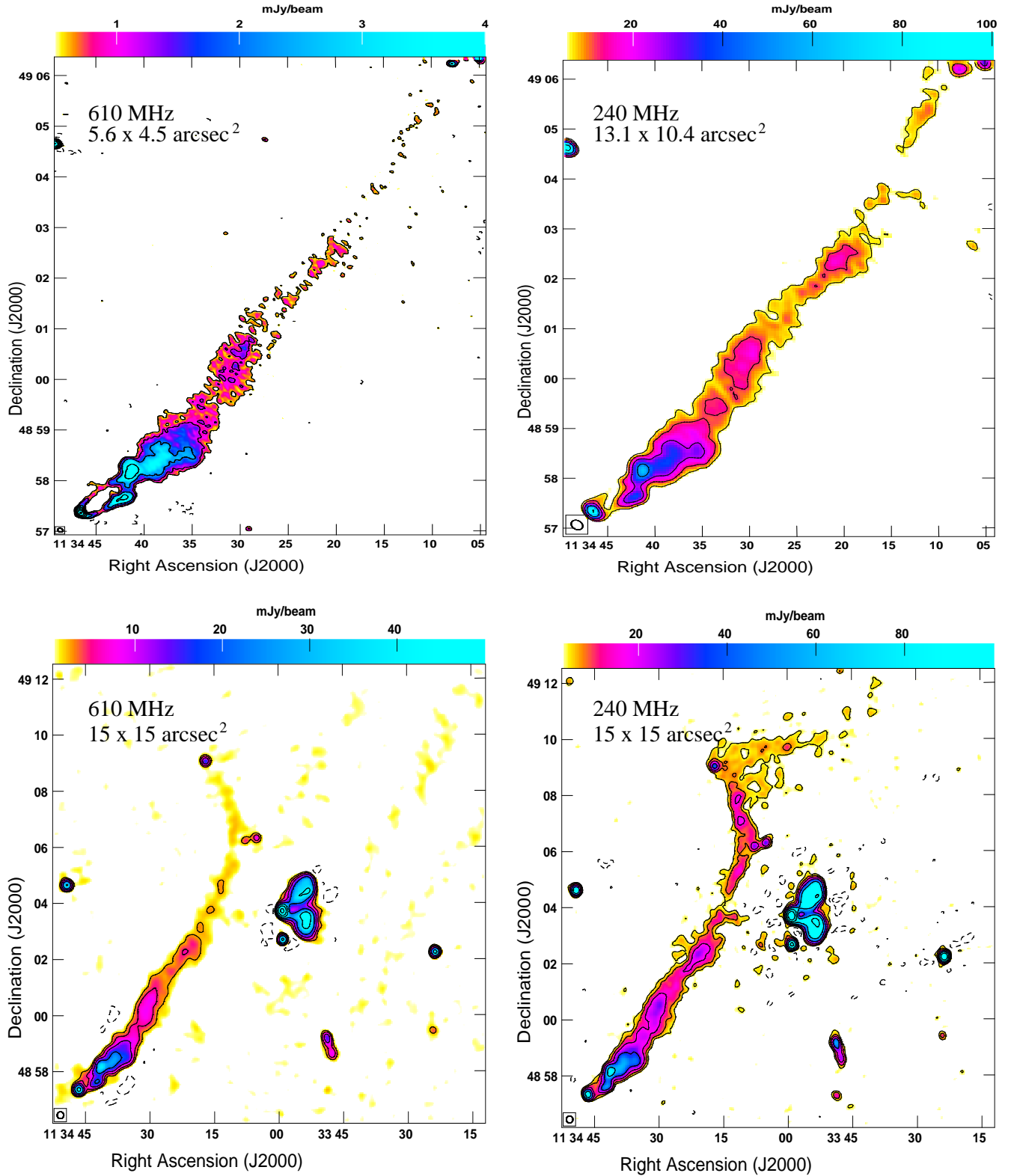


FIG. 7.— Full synthesis images of IC 711. Top left panel: image at 610 MHz with a beam size of $5''.6 \times 4''.5$ at a PA $-61^\circ.4$, the peak surface brightness is $36.2 \text{ mJy beam}^{-1}$, the error bar found at a source-free location is $0.1 \text{ mJy beam}^{-1}$ and the contour levels are $0.3 \times (-2, 2, 4, 8, 16, 32, 64, 128) \text{ mJy beam}^{-1}$. Top right panel: image at 240 MHz with a beam size of $13''.1 \times 10''.4$ at a PA $49^\circ.6$, the peak surface brightness is $98.3 \text{ mJy beam}^{-1}$, the error bar found at a source-free location is $0.9 \text{ mJy beam}^{-1}$ and the contour levels are $3.0 \times (-2, 2, 4, 8, 16, 32, 64, 128, 256) \text{ mJy beam}^{-1}$. Bottom left panel: low-resolution image at 610 MHz with a beam size of $15'' \times 15''$, the peak surface brightness is $195.0 \text{ mJy beam}^{-1}$, the error bar found at a source-free location is $0.6 \text{ mJy beam}^{-1}$ and the contour levels are $2.5 \times (-2, -1, 1, 2, 4, 8, 16, 32, 64) \text{ mJy beam}^{-1}$. Bottom right panel: low-resolution image at 240 MHz with a beam size of $15'' \times 15''$, the peak surface brightness is $508.0 \text{ mJy beam}^{-1}$, the error bar found at a source-free location is $0.9 \text{ mJy beam}^{-1}$ and the contour levels are $4.0 \times (-2, -1, 1, 2, 4, 8, 16, 32, 64) \text{ mJy beam}^{-1}$.

NGC 1265 in the Perseus cluster are two of the very well studied head–tail radio galaxies (Ryle & Windram 1968; Miley 1973; O’Dea & Owen 1986; Pfrommer & Jones 2011). The head is pointing toward the center of the cluster. The lower resolution images have picked up more diffuse emission than have the higher resolution images, as can be inferred from the contour maps (Figure 4). Sijbring & de Bruyn (1998) and Feretti et al. (1998) have imaged the sources in Perseus cluster at 1.4 GHz, 608 and 325 MHz. Their angular resolution is much coarser than in our maps. However, they have recovered more diffuse emission to the ends of the tails. Although they have mentioned about evidence for a faint twin tail in high-frequency VLA maps, the resolution of our maps does not seem to be enough to resolve them. The two tails are so well aligned that the two tails can just not be distinguished from each other. Since head–tail radio galaxies are seen in projection, it is hard to conclude if they are indeed head–tail sources or only appear to be head–tail sources in projection. However, there is a sudden increase in the surface brightness and apparent spatial extent of the tail as one moves along the jet. Recently IC 310 was detected in γ -ray emission bands in the gigaelectronvolt and teraelectronvolt energy ranges (Mariotti 2010). Aleksić et al. (2014) ruled out emission models occurring in a bow shock between the jet and the ICM, because of the day-scale variability in the very high-energy band, and seemed to favor the blazar-like scenario. Modeling of the spectral energy distribution of IC 310 suggested the peaking of the synchrotron emission at X-ray wavelengths and inverse-Compton radiation peaking in the multiteraelectronvolt band. Hence the source was classified as a high-frequency peaked BL LAC. IC 310 is the nearest known blazar and the brightest radio galaxy at TeV energies.

4.1.4. NGC 1265

The massive elliptical galaxy (O’Dea & Owen 1986, Figure 1) that marks the head of the radio galaxy appears to be directed toward the center of the cluster.

The high-resolution and low-resolution maps of NGC 1265 at 610 and 240 MHz are shown in Figure 5. O’Dea & Owen (1986) presented high frequency images of NGC 1265 and noted that the core possesses an inverted spectrum, which explains why the core is not quite conspicuous in our low-frequency maps while it appears quite prominent in their high-frequency maps. The individual jets are clearly seen to be launched at wide angles in the high-resolution maps at 610 MHz. Farther downstream, the jets appear to be bent by a very large angle, after which the jets expand in size and show higher surface brightness. Subsequently, the radio jets develop wiggles, which were first reported by O’Dea & Owen (1986). Sijbring & de Bruyn (1998) found extended emission to the northeastern side with low-frequency observations and coarser resolutions. This extension was found to have low surface brightness and a steep spectrum. Our map at 240 MHz, which has a comparatively higher resolution, recovers a part of this extended emission.

4.1.5. GB6 B0335+0955

Figure 1 shows that the elliptical host galaxy of GB6 B0335+0955 is located at the tip of the tail-like structure and is moving away from the cluster center.

Figure 6 shows the radio morphologies of the head–tail radio galaxy GB6 B0335+0955 at 610 and 240 MHz. The angular size of the galaxy is about $8'.5$. The core is prominent, and the individual jets are not resolved out. There is some evidence from the spatial profile of surface brightness near the core for a dip in surface brightness and a brightening later on. Farther down the tail, one notices an abrupt change in the direction of motion of the galaxy along with an increase in intensity. This could be because of interactions with neighboring galaxies that came close enough to cause deflection. Sarazin et al. (1995) suggested that this was due to buoyant motions of the tail following the low-density regions of the intergalactic medium. The steepening of the spectrum as the distance increases from the host galaxy is evident and is due to synchrotron aging of the radio-emitting plasma.

4.1.6. IC 711

IC 711 is the longest head–tail galaxy known (Vallee & Roger 1987; Vallee 1988; Vallee & Strom 1988). The high resolution maps of IC 711 at 610 and 240 MHz are presented in Figure 7. Thin, unresolved jets are seen to emerge from the radio core. Later on, both of the jets appear to widen into a high surface brightness feature, similar to a hot spot. The low-resolution images reveal much more extended features at the end of the tail. The galaxy seemed to have moved in an orbital trajectory, about the centroid of the cluster whose position is marked by the compact radio source IC 712 to the east of the radio tail. There is a sudden disruption toward the end of the tail. The low-resolution image at 240 MHz shows much more emission toward the extreme ends of the tails, pointing to comparatively high spectral index in that region. The morphology at the extreme ends of the tails suggests a not-so-simple circular motion around the cluster center (Srivastava & Singal 2016). However, it is also worth noting that the point sources that mark various twists and jerks in the smooth structure are not steep spectrum radio features, but instead are visible in both of the frequencies. Farther down the tail, the surface brightness drops, and the lower resolution image of IC 711 is similar to that of GB6 B0335+0955 and IC 310.

4.1.7. NGC 7385

The location of the host galaxy of NGC 7385 is shown in Figure 1. The position of the optical host galaxy is not coincident with the tip of the head–tail radio galaxy. This galaxy is a possible example where the jet direction is not perpendicular to the direction of the motion, as is seen in the classic examples of head–tail radio galaxies. However, the peculiar morphology may also be explained using projection effects, as was demonstrated by Reynolds (1980).

The radio maps of NGC 7385 at 610 and 240 MHz are presented in Figure 8. Hardee, Eilek & Owen (1980) had mapped this galaxy at 5 GHz using the VLA. The lower resolution images show much more extended structures. Although the spectral index steepens along the radio tail, the 240 MHz image at lower angular resolution does not show the diffuse emission toward the ends of the tails. This is because of the poor signal-to-noise ratio in the image, due to corruption from RFI. NGC 7385 is the only sample head–tail radio galaxy in which an optical jet

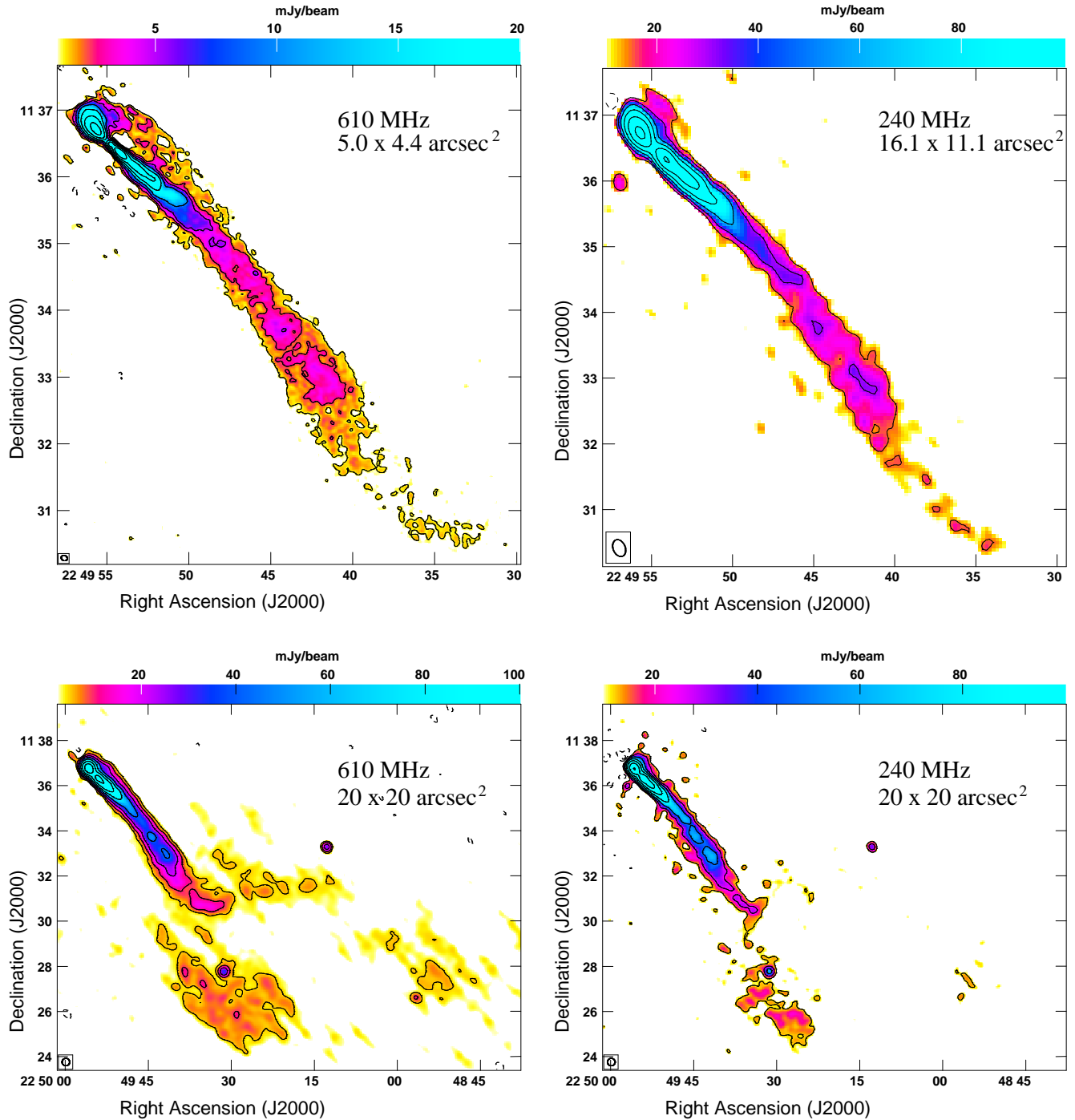


FIG. 8.— Full synthesis images of NGC 7385. Top left panel: image at 610 MHz with a beam size of $5''.0 \times 4''.4$ at a PA $-60^\circ.2$, the peak surface brightness is $146.2 \text{ mJy beam}^{-1}$, the error bar found at a source-free location is $0.2 \text{ mJy beam}^{-1}$ and the contour levels are $1.2 \times (-2, -1, 1, 2, 4, 8, 16, 32, 64) \text{ mJy beam}^{-1}$. Top right panel: image at 240 MHz with a beam size of $16''.1 \times 11''.1$ at a PA $-22^\circ.1$, the peak surface brightness is $573.0 \text{ mJy beam}^{-1}$, the error bar found at a source-free location is $2.0 \text{ mJy beam}^{-1}$ and the contour levels are $15.0 \times (-1, 1, 2, 4, 8, 16, 32, 64) \text{ mJy beam}^{-1}$. Bottom left panel: low-resolution image at 610 MHz with a beam size of $20'' \times 20''$, the peak surface brightness is $461.3 \text{ mJy beam}^{-1}$, the error bar found at a source-free location is $1.4 \text{ mJy beam}^{-1}$ and the contour levels are $6.0 \times (-2, -1, 1, 2, 4, 8, 16, 32, 64) \text{ mJy beam}^{-1}$. Bottom right panel: low-resolution image at 240 MHz with a beam size of $20'' \times 20''$, the peak surface brightness is $667.8 \text{ mJy beam}^{-1}$, the error bar found at a source-free location is $2.3 \text{ mJy beam}^{-1}$ and the contour levels are $12.0 \times (-2, -1, 1, 2, 4, 8, 16, 32, 64, 128) \text{ mJy beam}^{-1}$.

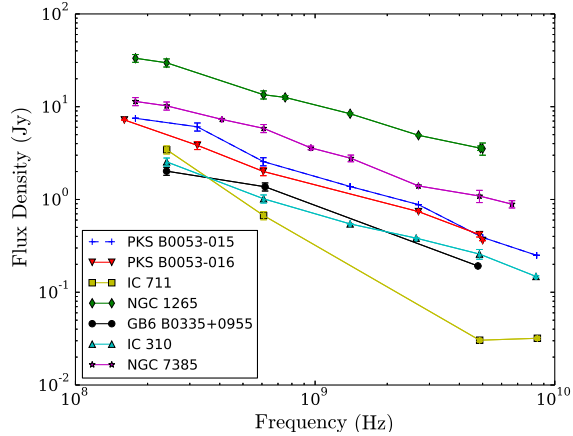


FIG. 9.— Integrated flux densities all sources in the sample. The GMRT flux density measurements at 240 MHz and 610 MHz are in good agreement with the data at close frequencies taken from the literature. The error bars of the GMRT flux density measurements are quoted in respective Figures (from Figure 2 to Figures 8).

and also an X-ray jet were detected (Rawes, Worrall & Birkinshaw 2015).

4.2. Spectral structure and physical parameters

A population of relativistic electrons following a power law distribution of energies in the presence of a magnetic field will emit synchrotron radiation, which follows a power-law in frequency. According to synchrotron theory, the rate of energy loss of a radiating electron is proportional to the square of the energy of the electron. Therefore, high-energy electrons lose energy faster and get depleted earlier than low-energy ones. This depletion of high-energy electrons produces a break in the synchrotron spectrum, which moves to lower frequencies as time elapses. The spectrum also becomes steeper. In FRI radio galaxies, the electron population toward the end of the tail are much older than that near the radio core since there is a constant injection of a fresh population of electrons near the core. Additionally, the head–tail galaxies are moving through the ICM with a velocity comparable to the speed of the radio jet, as inferred from the bending (O’Dea 1985). The synchrotron-emitting plasma at the ends of the radio tails thus is stationary with respect to the ICM. Hence (1) it is harder for the newly injected electron population in head–tail radio galaxies to reach the ends of the radio tails, and (2) the spectral steepening in head–tail radio galaxies is expected to be more pronounced than in normal FRI radio galaxies.

In order to calculate the rest-frame radio power, $L_{610 \text{ MHz}}$, we used the spectral index α between 240/325 and 610 MHz (Figure 9) and

$$L_{610 \text{ MHz}} = 4\pi D_L^2(z) \int S_\nu d\nu,$$

where $D_L(z)$ is the luminosity distance and $S_{610 \text{ MHz}}$ is the flux density at 610 MHz.

The role played by magnetic fields in the evolution and dynamics of head–tail galaxies is barely explored. Due to limited data, we estimate magnitudes of magnetic fields using the minimum energy conditions (Burbidge 1956). The head–tail galaxies were divided into

several regions of rectangular shape perpendicular to the length of the tail, and the volumes of these regions were calculated assuming a cylindrical geometry. Note that this could lead to underestimation, especially in cases where one of the tails lies over the other in projection. We assume the electron population to radiate at frequencies from 10^7 Hz to 10^{10} Hz and we further assume that one-half of the total energy of the particles is carried by electrons. We measure the total flux densities from both 240 and 610 MHz maps and determine spectral indices for every region and estimate the equipartition magnetic field. A calibration error of 10% was assumed on flux density and was added to the RMS noise of the intensity maps in quadrature. Following Moffet (1975), we calculate the equipartition magnetic field B_{eq} using

$$B_{\text{eq}} = 2.3(aAL/V)^{2/7};$$

where a , A , L and V are the fraction of total energy in protons to that in electrons, the shape factor, the total radio power, and the volume of the region, respectively. The radio spectra and the equipartition magnetic field as a function of distance from the head are plotted in Figure 10. There is a clear decrease in the spectral index and in the magnetic field values as one moves away from the core. Furthermore, the spectral index steepens when moving away from the center in all but two sources, IC 310 and IC 711 (Figure 10). Briefly, the electron population in the tails loses a significant amount of its energy by radiation. If the particles are in equipartition, then the total energy will be shared almost equally as magnetic field energy and electron energy. Hence the equipartition magnetic field becomes weaker with distance from the head. The profile of the minimum pressure,

$$P_{\text{eq}} = U_{\text{min}}/3$$

mimics the profile of the equipartition magnetic field of the radio plasma.

We also derive the upper limit to the radiative age, assuming a magnetic field $B_{\text{IC}} = 4(1+z)^2 \mu\text{G}$, of the synchrotron-emitting electrons at these regions shown in Figure 10 using

$$t = 1060 \frac{B^{0.5}}{(B^2 + B_{\text{IC}}^2)} [(1+z)\nu_{\text{br}}]^{-0.5} \text{ Myr}.$$

Here, the frequency where the radio spectrum changes by 0.5 is the break frequency, ν_{br} , in GHz, and the magnetic fields, B and B_{IC} , are in μG (Miley 1980). Due to sparse radio frequency measurements of the spatially resolved structures for our sample sources, we assume $\nu_{\text{br}} = 1420$ MHz.

We present the measured source properties at the sampled locations for each of our sample sources in Table 2 including distance from the head along the tail (column 1), size (column 2), radio luminosity (column 3), spectral index between 240 MHz (or 325 MHz) and 610 MHz (column 4), equipartition parameters (from columns 5 to column 7) and radiative age (column 8). Below we provide a description of the spectral structure shown in Figure 10 from the radio morphologies at 240/325 and 610 MHz discussed above for our sample sources. Also presented in Figure 10 are profiles of the equipartition parameters and spectral index of the

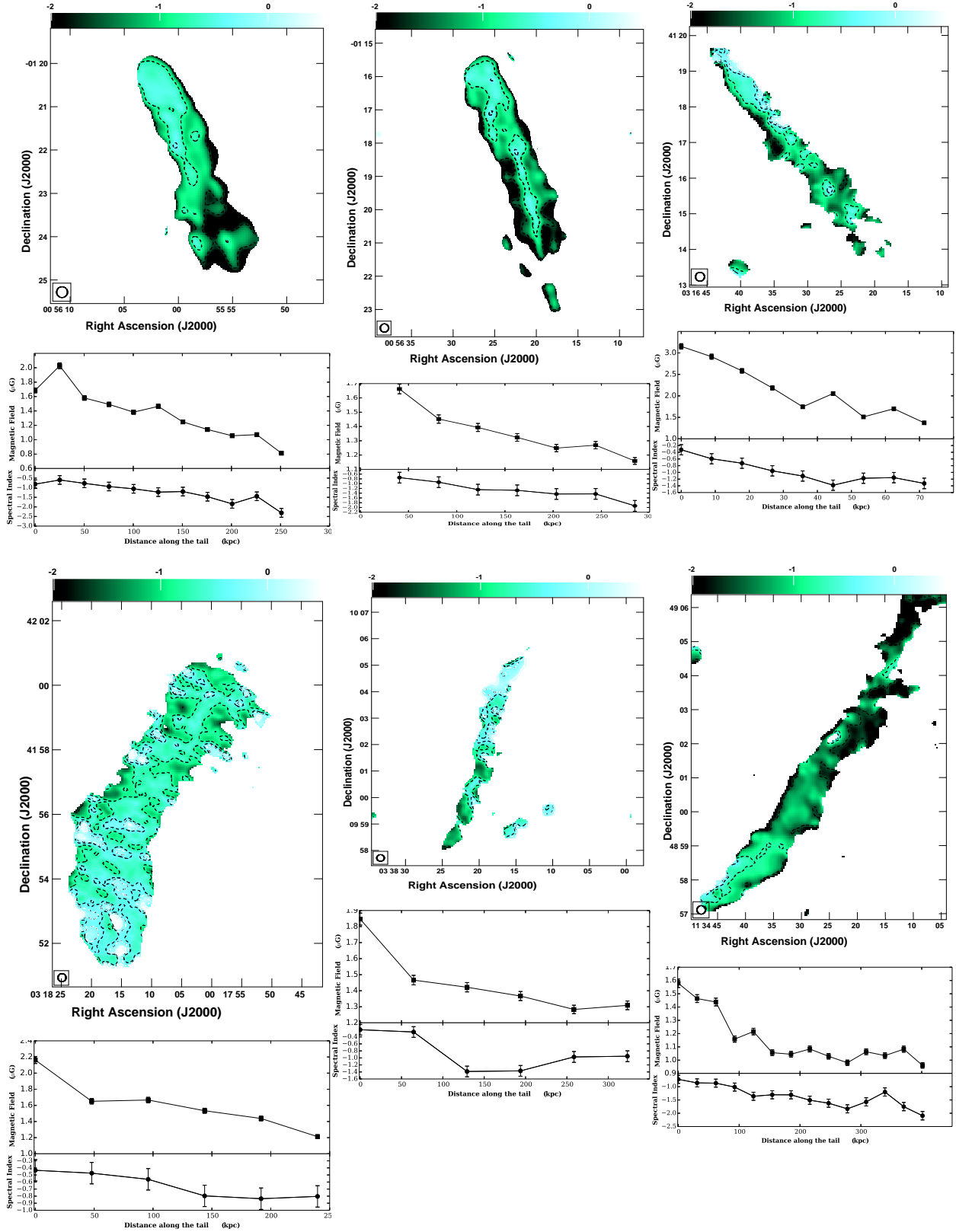


FIG. 10.— Upper panel: distribution of spectral indices between 240/325 and 610 MHz for PKS B0053–016 (left panel), PKS B0053–015 (middle panel) and IC 310 (right panel). Lower panel: distribution of spectral indices, between 240 MHz and 610 MHz for NGC 1265 (left panel), GB6 B0335+0955 (middle panel) and IC 711 (right panel). The corresponding panels below them are profiles of the equipartition magnetic fields (upper panel) and spectral index (lower panel) of the radio emitting plasma along the tail from the head at the sampled positions of the radio galaxy. In the spectral index maps, the lighter regions represent the relatively flat spectrum regions as compared to the darker regions which represent the steep spectrum. The profile of the minimum pressure (not plotted; also see Table 2), mimics the profile of the equipartition magnetic field of the radio plasma.

radio-emitting plasma along the tail from the head at the sample positions of the radio galaxy.

4.2.1. *PKS B0053–016*

The spectral index value steepens from -0.82 in the region near the core to -2.31 toward the farthest end of the tail. Apart from the steepening of the spectral index, Feretti et al. (1999) also finds evidence for a spectral curvature in the tails at about a distance of $2'$ away from the core. Both the steepening and the presence of spectral curvature are consistent with the aging of the plasma toward the ends of the tails. Figure 10 shows that there is an increase in the spectral index next to the core. Although this discontinuity in the steepening trend of the spectral index just after the core is within the error bars, there are certain factors worth noticing. The surface brightness of the radio plasma in this region suddenly increases and then decreases downstream, as can be inferred from Table 2. The flatter spectrum compared to that near the core indicates that some of the electrons were pushed to higher energies. The net increase in energy of the electrons leads to an increase in energy stored in the magnetic field if minimum energy conditions hold true. This leads to the noticeable change in the trend in the magnetic field. There is a weak discontinuity in the magnetic field farther downstream even though there are no such signatures in the spectral index variation. This is probably due to an underestimation of the volume and may not be a real physical trend.

4.2.2. *PKS B0053–015*

Although the spectral index and magnetic field steepen without any noticeable discontinuities, the spectral index map shows several interesting features. In almost all the head–tail galaxies presented here, there is a steepening trend in the spectral index as one traverses away from the head along the tail.

But, in PKS 0053–015, there is a region where a narrow filament of less-steep plasma seems to be embedded in a steeper background. The surface brightness maps (see Figure 3) show that the narrow flat spectrum filament coincides with the jet that is directed toward the south, while the diffuser background is more likely to correspond to the jet that is directed northward. They may not be spatially coinciding but appear so in projection. This difference in the spectral index points to differently aged electron populations. The fact that the steep background that corresponds to the northern jet is more extended also points toward a more dynamical evolution. Also, in Section 4.1.2 it was pointed out that the jets are launched at an angle smaller than 90° with the direction of motion of the galaxy. Hence, the difference in the ages of the plasma indicates that this peculiar orientation of jets must have remained the same throughout the entire duration when the host galaxy traversed the length of the radio emission, which represents its past trajectory.

4.2.3. *IC 310*

The core has a low spectral index value of -0.33 . We find that as one moves farther away from the core, the spectral index steepens, consistent with earlier results by Feretti et al. (1998) and Sijbring & de Bruyn (1998). Un-

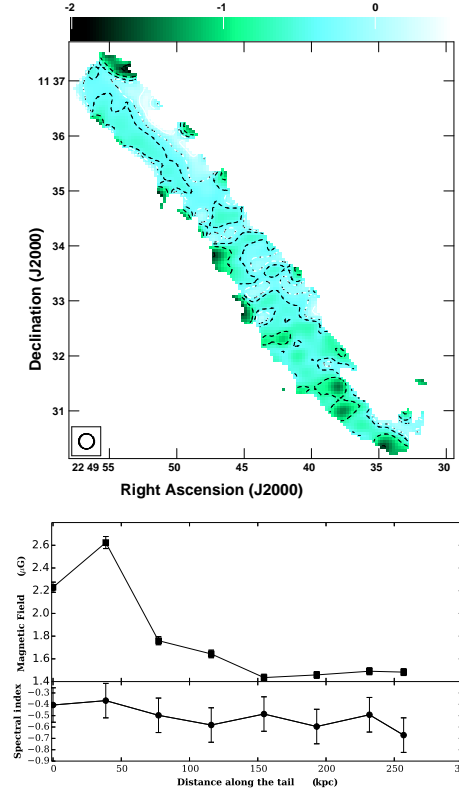


FIG. 10.— *Continued* – The distribution of spectral indices, between 240 MHz and 610 MHz for NGC 7385 .

like in PKS 0053–016, the spectral index does not flatten at the position of the flare. This might be because the first region at the core is dominated by the emission from the compact core instead of the jet, and hence the difference in spectral index between the first and second regions is barely noticeable. In PKS 0053–016, the emission from the compact core is not very prominent. Figure 10 shows that there is a discontinuity in the decreasing trend in the magnetic field seen farther downstream. It is noticeable that the spectral index decreases at the location of this discontinuity. The steady steepening of the spectral index despite an increase in the magnetic field indicates that there are no reacceleration processes playing a role in this region. Table 2 for IC 310 shows that the net luminosity emitted is comparable to that in the other regions but from a much smaller volume. Hence, this discontinuity in the magnetic field most probably arises because of the projection effects that lead to uncertainties while measuring the volume. Toward the end of the tail, beyond 45 kpc, we find a discontinuity in the trend of the spectral index, where it starts to rise after a small dip and thereafter falls again. It is unlikely that this is happening because of uncertainties in imaging the diffuse structure because, had it been the case, the lower-frequency images will pick up more flux from diffuse structures because of better uv coverage and hence show an artificial steepening trend instead of flattening.

4.2.4. *NGC 1265*

The overall steepening of the spectral index toward the tail is perceivable in both the spectral index map and

TABLE 2

DISTANCE FROM THE HEAD ALONG THE TAIL, SIZE, RADIO LUMINOSITY, AND EQUIPARTITION PARAMETERS ALONG WITH RADIATIVE AGE AT THE SAMPLED POSITION FOR THE SAMPLE SOURCE CALCULATED FOLLOWING THE FORMALISM EXPLAINED IN SECT. 5.

| Distance (kpc) (1) | Size (cm^{-3}) (2) | Luminosity (erg s^{-1}) (3) | α (4) | B_{\min} (μG) (5) | U_{\min} (erg cm^{-3}) (6) | P_{\min} (dyne cm^{-2}) (7) | Age (Myr) (8) |
|--------------------------|-------------------------------------|--|-----------------|--|---|--|---------------------|
| PKS 0053–016 | | | | | | | |
| 0.0 | 6.5×10^{68} | $2.3 \pm 0.3 \times 10^{39}$ | -0.82 | 1.7 | $11.3 \pm 0.5 \times 10^{-14}$ | 3.8×10^{-14} | 52.2 |
| 25.1 | 12.3×10^{68} | $8.0 \pm 1.2 \times 10^{39}$ | -0.60 | 2.0 | $16.4 \pm 0.7 \times 10^{-14}$ | 5.5×10^{-14} | 53.9 |
| 50.2 | 16.6×10^{68} | $4.6 \pm 0.8 \times 10^{39}$ | -0.77 | 1.6 | $9.9 \pm 0.4 \times 10^{-14}$ | 3.3×10^{-14} | 51.5 |
| 75.3 | 15.6×10^{68} | $3.4 \pm 0.5 \times 10^{39}$ | -0.94 | 1.5 | $8.9 \pm 0.4 \times 10^{-14}$ | 3.0×10^{-14} | 50.6 |
| 100.4 | 16.9×10^{68} | $2.9 \pm 0.5 \times 10^{39}$ | -1.06 | 1.4 | $7.6 \pm 0.3 \times 10^{-14}$ | 2.5×10^{-14} | 49.5 |
| 125.4 | 13.2×10^{68} | $2.9 \pm 0.6 \times 10^{39}$ | -1.23 | 1.5 | $8.5 \pm 0.4 \times 10^{-14}$ | 2.8×10^{-14} | 50.6 |
| 150.5 | 19.3×10^{68} | $2.4 \pm 0.4 \times 10^{39}$ | -1.20 | 1.3 | $6.2 \pm 0.3 \times 10^{-14}$ | 2.1×10^{-14} | 48.3 |
| 175.6 | 21.6×10^{68} | $1.9 \pm 0.3 \times 10^{39}$ | -1.47 | 1.1 | $5.2 \pm 0.2 \times 10^{-14}$ | 1.7×10^{-14} | 45.5 |
| 200.7 | 28.6×10^{68} | $1.8 \pm 0.4 \times 10^{39}$ | -1.84 | 1.1 | $4.4 \pm 0.2 \times 10^{-14}$ | 1.5×10^{-14} | 45.5 |
| 225.8 | 32.2×10^{68} | $2.2 \pm 0.4 \times 10^{39}$ | -1.45 | 1.1 | $4.6 \pm 0.2 \times 10^{-14}$ | 1.5×10^{-14} | 45.5 |
| 250.9 | 32.9×10^{68} | $9.4 \pm 1.6 \times 10^{38}$ | -2.31 | 0.8 | $2.6 \pm 0.1 \times 10^{-14}$ | 0.9×10^{-14} | 40.0 |
| PKS 0053–015 | | | | | | | |
| 0.0 | 2.3×10^{69} | $7.6 \pm 1.1 \times 10^{39}$ | -0.75 | 1.7 | $1.10 \pm 0.5 \times 10^{-14}$ | 0.3×10^{-14} | 53.0 |
| 40.7 | 3.7×10^{69} | $7.5 \pm 1.2 \times 10^{39}$ | -0.94 | 1.5 | $8.4 \pm 0.3 \times 10^{-14}$ | 2.8×10^{-14} | 51.3 |
| 81.3 | 3.2×10^{69} | $5.9 \pm 1.1 \times 10^{39}$ | -1.25 | 1.4 | $7.7 \pm 0.3 \times 10^{-14}$ | 2.6×10^{-14} | 50.3 |
| 122.0 | 2.9×10^{69} | $4.3 \pm 0.8 \times 10^{39}$ | -1.28 | 1.3 | $7.0 \pm 0.3 \times 10^{-14}$ | 2.3×10^{-14} | 49.1 |
| 162.7 | 3.1×10^{69} | $3.8 \pm 0.7 \times 10^{39}$ | -1.44 | 1.3 | $6.2 \pm 0.3 \times 10^{-14}$ | 2.1×10^{-14} | 49.1 |
| 203.4 | 3.0×10^{69} | $3.8 \pm 0.8 \times 10^{39}$ | -1.43 | 1.3 | $6.4 \pm 0.3 \times 10^{-14}$ | 2.1×10^{-14} | 49.1 |
| 244.0 | 3.0×10^{69} | $2.8 \pm 0.5 \times 10^{39}$ | -1.93 | 1.2 | $5.3 \pm 0.2 \times 10^{-14}$ | 1.8×10^{-14} | 47.7 |
| IC 310 | | | | | | | |
| 0.0 | 1.2×10^{68} | $6.4 \pm 2.0 \times 10^{38}$ | -0.33 | 1.9 | $15.1 \pm 0.6 \times 10^{-14}$ | 5.0×10^{-14} | 58.2 |
| 17.4 | 1.8×10^{68} | $10.6 \pm 2.7 \times 10^{38}$ | -0.59 | 2.0 | $16.4 \pm 0.6 \times 10^{-14}$ | 5.5×10^{-14} | 58.7 |
| 36.4 | 1.8×10^{68} | $8.1 \pm 2.2 \times 10^{38}$ | -0.73 | 1.8 | $13.3 \pm 0.5 \times 10^{-14}$ | 4.4×10^{-14} | 57.7 |
| 55.5 | 2.0×10^{68} | $3.6 \pm 1.2 \times 10^{38}$ | -0.95 | 1.4 | $8.1 \pm 0.3 \times 10^{-14}$ | 2.7×10^{-14} | 54.3 |
| 74.5 | 3.3×10^{68} | $3.7 \pm 0.8 \times 10^{38}$ | -1.11 | 1.2 | $6.2 \pm 0.2 \times 10^{-14}$ | 2.1×10^{-14} | 51.7 |
| 93.5 | 2.2×10^{68} | $3.5 \pm 0.6 \times 10^{38}$ | -1.38 | 1.3 | $7.2 \pm 0.2 \times 10^{-14}$ | 2.4×10^{-14} | 53.1 |
| 112.0 | 5.0×10^{68} | $3.6 \pm 0.6 \times 10^{38}$ | -1.17 | 1.1 | $5.0 \pm 0.2 \times 10^{-14}$ | 1.7×10^{-14} | 50.1 |
| 131.5 | 3.8×10^{68} | $2.9 \pm 0.5 \times 10^{38}$ | -1.16 | 1.1 | $4.9 \pm 0.2 \times 10^{-14}$ | 1.6×10^{-14} | 50.1 |
| 150.0 | 3.6×10^{68} | $1.6 \pm 0.3 \times 10^{38}$ | -1.33 | 0.9 | $3.9 \pm 0.1 \times 10^{-14}$ | 1.3×10^{-14} | 46.3 |
| NGC 1265 | | | | | | | |
| 0.0 | 2.9×10^{69} | $2.2 \pm 0.5 \times 10^{40}$ | -0.43 | 2.2 | $18.6 \pm 0.8 \times 10^{-14}$ | 6.2×10^{-14} | 57.9 |
| 47.9 | 7.0×10^{69} | $2.1 \pm 0.4 \times 10^{40}$ | -0.47 | 1.7 | $10.8 \pm 0.4 \times 10^{-14}$ | 3.6×10^{-14} | 55.7 |
| 95.9 | 5.0×10^{69} | $1.5 \pm 0.3 \times 10^{40}$ | -0.56 | 1.7 | $11.1 \pm 0.5 \times 10^{-14}$ | 3.7×10^{-14} | 55.7 |
| 143.8 | 4.5×10^{69} | $1.0 \pm 0.2 \times 10^{40}$ | -0.80 | 1.5 | $9.4 \pm 0.4 \times 10^{-14}$ | 3.1×10^{-14} | 54.0 |
| 191.8 | 4.9×10^{69} | $9.0 \pm 1.5 \times 10^{39}$ | -0.84 | 1.4 | $8.2 \pm 0.3 \times 10^{-14}$ | 2.7×10^{-14} | 53.0 |
| 239.7 | 8.2×10^{69} | $8.3 \pm 1.5 \times 10^{39}$ | -0.80 | 1.2 | $5.8 \pm 0.2 \times 10^{-14}$ | 1.9×10^{-14} | 50.4 |
| GB6 B0335+0955 | | | | | | | |
| 0.0 | 1.5×10^{69} | $7.1 \pm 1.4 \times 10^{39}$ | -0.20 | 1.9 | $13.6 \pm 0.6 \times 10^{-14}$ | 4.5×10^{-14} | 54.2 |
| 64.6 | 2.5×10^{69} | $4.8 \pm 1.0 \times 10^{39}$ | -0.26 | 1.5 | $8.6 \pm 0.4 \times 10^{-14}$ | 2.9×10^{-14} | 51.3 |
| 129.3 | 1.5×10^{69} | $3.7 \pm 0.6 \times 10^{39}$ | -1.39 | 1.4 | $8.0 \pm 0.3 \times 10^{-14}$ | 2.7×10^{-14} | 50.3 |
| 193.9 | 1.3×10^{69} | $2.2 \pm 0.4 \times 10^{39}$ | -1.37 | 1.4 | $7.4 \pm 0.3 \times 10^{-14}$ | 2.5×10^{-14} | 50.3 |
| 258.6 | 1.5×10^{69} | $1.8 \pm 0.4 \times 10^{39}$ | -0.97 | 1.3 | $6.6 \pm 0.3 \times 10^{-14}$ | 2.2×10^{-14} | 49.1 |
| 323.2 | 1.1×10^{69} | $1.3 \pm 0.2 \times 10^{39}$ | -0.95 | 1.3 | $6.8 \pm 0.3 \times 10^{-14}$ | 2.3×10^{-14} | 49.1 |
| IC 711 | | | | | | | |
| 0.0 | 3.3×10^{68} | $7.9 \pm 1.8 \times 10^{38}$ | -0.72 | 1.6 | $9.9 \pm 0.4 \times 10^{-14}$ | 3.3×10^{-14} | 53.4 |
| 30.9 | 7.3×10^{68} | $13.9 \pm 2.6 \times 10^{38}$ | -0.86 | 1.5 | $8.5 \pm 0.4 \times 10^{-14}$ | 2.8×10^{-14} | 52.5 |
| 61.7 | 13.7×10^{68} | $24.0 \pm 5.0 \times 10^{38}$ | -0.87 | 1.4 | $8.2 \pm 0.3 \times 10^{-14}$ | 2.7×10^{-14} | 51.4 |
| 92.6 | 18.8×10^{68} | $15.8 \pm 3.3 \times 10^{38}$ | -1.01 | 1.2 | $5.3 \pm 0.2 \times 10^{-14}$ | 1.8×10^{-14} | 48.9 |
| 123.5 | 7.9×10^{68} | $7.8 \pm 1.6 \times 10^{38}$ | -1.36 | 1.2 | $5.9 \pm 0.2 \times 10^{-14}$ | 2.0×10^{-14} | 48.9 |
| 154.4 | 18.1×10^{68} | $10.9 \pm 2.0 \times 10^{38}$ | -1.30 | 1.1 | $4.4 \pm 0.2 \times 10^{-14}$ | 1.5×10^{-14} | 47.4 |
| 185.2 | 13.7×10^{68} | $8.0 \pm 1.4 \times 10^{38}$ | -1.31 | 1.0 | $4.3 \pm 0.2 \times 10^{-14}$ | 1.4×10^{-14} | 45.6 |
| 216.1 | 7.0×10^{68} | $4.7 \pm 0.8 \times 10^{38}$ | -1.51 | 1.1 | $4.7 \pm 0.2 \times 10^{-14}$ | 1.6×10^{-14} | 47.4 |
| 245.0 | 11.7×10^{68} | $6.2 \pm 1.3 \times 10^{38}$ | -1.62 | 1.0 | $4.2 \pm 0.2 \times 10^{-14}$ | 1.4×10^{-14} | 45.6 |
| 277.9 | 12.1×10^{68} | $5.7 \pm 1.1 \times 10^{38}$ | -1.83 | 1.0 | $3.8 \pm 0.2 \times 10^{-14}$ | 1.3×10^{-14} | 45.6 |
| 308.7 | 5.1×10^{68} | $3.0 \pm 0.6 \times 10^{38}$ | -1.57 | 1.1 | $4.5 \pm 0.2 \times 10^{-14}$ | 1.5×10^{-14} | 47.4 |
| 339.6 | 4.4×10^{68} | $2.3 \pm 0.8 \times 10^{38}$ | -1.20 | 1.0 | $4.3 \pm 0.2 \times 10^{-14}$ | 1.4×10^{-14} | 45.6 |
| 370.5 | 4.3×10^{68} | $2.9 \pm 0.7 \times 10^{38}$ | -1.75 | 1.1 | $4.7 \pm 0.2 \times 10^{-14}$ | 1.6×10^{-14} | 47.4 |
| 401.4 | 5.4×10^{68} | $2.2 \pm 0.5 \times 10^{38}$ | -2.09 | 1.0 | $3.7 \pm 0.2 \times 10^{-14}$ | 1.2×10^{-14} | 45.6 |
| NGC 7385 | | | | | | | |
| 0.0 | 11.3×10^{68} | $9.7 \pm 2.3 \times 10^{39}$ | -0.41 | 2.2 | $19.8 \pm 0.8 \times 10^{-14}$ | 6.6×10^{-14} | 57.7 |
| 38.6 | 4.9×10^{68} | $7.3 \pm 1.5 \times 10^{39}$ | -0.37 | 2.6 | $27.4 \pm 1.1 \times 10^{-14}$ | 9.1×10^{-14} | 57.8 |
| 77.3 | 6.8×10^{68} | $2.7 \pm 0.5 \times 10^{39}$ | -0.50 | 1.8 | $12.3 \pm 0.5 \times 10^{-14}$ | 4.1×10^{-14} | 56.1 |
| 115.9 | 7.4×10^{68} | $2.3 \pm 0.4 \times 10^{39}$ | -0.58 | 1.6 | $10.7 \pm 0.4 \times 10^{-14}$ | 3.6×10^{-14} | 54.7 |
| 154.5 | 1.4×10^{69} | $2.6 \pm 0.5 \times 10^{39}$ | -0.49 | 1.4 | $8.2 \pm 0.3 \times 10^{-14}$ | 2.7×10^{-14} | 52.7 |
| 193.2 | 8.9×10^{68} | $1.7 \pm 0.2 \times 10^{39}$ | -0.60 | 1.5 | $8.5 \pm 0.3 \times 10^{-14}$ | 2.8×10^{-14} | 53.8 |
| 231.8 | 5.7×10^{68} | $1.1 \pm 0.2 \times 10^{39}$ | -0.49 | 1.5 | $8.9 \pm 0.4 \times 10^{-14}$ | 3.0×10^{-14} | 53.8 |
| 256.9 | 5.7×10^{68} | $1.2 \pm 0.3 \times 10^{39}$ | -0.67 | 1.5 | $8.8 \pm 0.4 \times 10^{-14}$ | 2.9×10^{-14} | 53.8 |

the spectral index versus distance plot (Figure 10). This trend was previously observed by Jaegers (1987), Feretti et al. (1998) and Sijbring & de Bruyn (1998) at higher frequencies. The spectral index varies from -0.43 at the host galaxy to -0.8 at the tip of the detected tail. The trend is quite smooth in both the magnetic field plot and the spectral index plot. However, the spectral index map shows that the edges of the tails show a slightly steeper spectral index than the ridge line. This might be an aftereffect of the reacceleration caused by the interaction between the two separate tails at the center. This might also arise because of the systematic deconvolution errors introduced while cleaning. The spectral index plot does not show a steepening trend after about 150 kpc. However, the errors are quite high in this case, and hence we may not be justified in favoring a flatter spectrum toward the end of the tail.

4.2.5. GB6 B0335+0955

The spectral index map and its variation with the distance are shown in Figure 10. Though the intensity maps show a sudden increase in intensity near the core, it is evident from the values in Table 2 that the core region is much more luminous than the second brightness peak. The brightness peak is several tens of kiloparsecs away from the core. The spectral index is low at the core, with a spectral index value of -0.2 . The spectral index at the nearby, bright blob-like feature is also quite flat, with a spectral index of about -0.26 . This is very unusual for a synchrotron-aged plasma unless it is being reaccelerated by some other mechanisms. The slight change in direction of the tails at the point raises suspicions that this is an aftereffect of gravitational interaction with a neighboring galaxy.

Sarazin et al. (1995) also finds this steepening in the spectra. Their spectral index values range from -1.27 to -2.02 . Their spectral index values are bigger than ours probably because the values were calculated from high-frequency (between 1.4 and 4.88 GHz) maps, and hence a break might have occurred. The total extent of the galaxy is also smaller compared to our maps. The field is quite crowded, and the high-frequency images show many other sources overlapping the tail. The steady steepening trend that is usually seen in head–tail galaxies is not seen in this galaxy. Although there is a rising trend in the spectral index, the net luminosity is decreasing consistently along the tail.

4.2.6. IC 711

Figure 10 shows the spectral index map of IC 711. The spectral index varies from -0.7 at the core to -2.0 toward the end of the tail. The discrepancy in the trend of the spectral index at about 350 kpc away from the head was noted by Wilson & Vallee (1977). They concluded this was happening because of the acceleration of the particles or the injection of the energy from any other external agency. But from our current understanding of radio galaxies, it is extremely unlikely that an external source provides energy to the tail. Though the spectrum is flatter compared to the nearby regions, the net luminosity from this region follows a smooth decreasing trend. This implies that, instead of an increase in the total energy, the flattening of the spectral index is a result

of the redistribution of energies of the electron population. This might be induced by some turbulence due to the gravitational influence of nearby massive galaxies like IC 708, which appears to be very close to this part of the tail.

4.2.7. NGC 7385

Schilizzi & Ekers (1975) have studied the variation of the spectral index along the tail of this head–tail galaxy and have noted the progressive increase in the spectral index, with the maximum value of the spectral index reaching up to -1.0 . Figure 10 shows the spectral index map and its variation with distance along with the variation of the magnetic field with distance. Note that NGC 7385 is one of the galaxies in the sample with a misplaced optical host. The second point in the plot hence corresponds to the region which includes the core and is flatter compared to the first and the third point. This also leads to a sudden increase in the equipartition magnetic field. The signal-to-noise ratio was not high enough to obtain the spectral index values of the extended structures with the low surface brightness. The range of the spectral index is from -0.37 near the core to -0.67 at the end.

5. DISCUSSION

Seven head–tail radio sources have been mapped in detail with an angular-scale resolution of $\sim 5''$ – $20''$.

5.1. General source properties

All the head–tail galaxies have so far been found exclusively in clusters, and in most cases in rich clusters. Since the morphology of head–tail radio galaxies is thought to be a result of the ram pressure that is due to the relative motion of the radio galaxy through the ICM (Miley et al. 1972; Bliton et al 1998), fitting the bending of the trajectory of jets using beam models (Begelman et al. 1979; Jones & Owen 1979; Baan & McKee 1985) gives estimates of several parameters, such as the jet flow velocity and the initial ejection angle of the jet with respect to the motion of the galaxy. Hence, the hypotheses that host galaxy orbits are either radial, circular, or isotropic are tested, and the hypothesis that head–tail radio galaxies are primarily (or the inward portion of them) in highly elliptical orbits (Jones & Owen 1979) is also tested. Observationally, images at higher angular resolution are needed to do such analyses. Since most of the head–tail radio galaxies in the sample are narrow-angle tail (NAT) sources, the two jets are just not distinguishable, such as in three of the seven sources in our sample. Furthermore, the probability of projection effects to be playing a major role is large, and it becomes difficult to decouple the projection effects and the trajectory of the jets. In the light of our data for the sample sources and our understanding from the literature, below we present arguments to state that (1) the bending of radio tails is due to the motion of the host galaxy through the ICM, (2) these galaxies have an isotropic distribution of the orientations about the cluster center, (3) the asymmetries seen in the intensity profiles of the radio jets in some of the head–tail radio galaxies are due to the difference in environments along with the projection effects and the ejection of jets at acute angles with respect to the direction of motion

of the host galaxy through the ICM, and (4) the multiple bends and wiggles are possibly due to the precessing radio jets.

It was previously noted by Eilek et al. (1984), Burns et al. (1982), and Burns (1981) that the bending in radio jets seen in wide-angle tail (WAT) radio sources could not be explained by the usual ram pressure bending models. This is because these galaxies are usually seen to be associated with the cluster dominant galaxies, which would have low velocities against the ICM gas. However, five out of the seven sources in our sample are part of rich, cool core clusters and are seen to be at a range of distances from the brightest cluster galaxy. Although IC 711 and NGC 7385 are not part of rich clusters, they are not associated with the dominant and the most massive galaxy of their respective clusters. We therefore expect that all of the galaxies in our sample would have high velocities around their cluster center potentials. As a result, the bending of the tails is entirely possibly due to the motion of the host galaxy through the ICM.

According to ram pressure bending models, the radio trails trace the motion of the galaxy through the cluster. In a random sample of galaxies in a cluster, one expects random directions of motion of galaxies. We find that NGC 1265 and IC 310 are directed toward NGC 1275, the cD galaxy in the Perseus cluster. PKS B0053–016 is also almost directed toward the cluster center. GB6 B0335+0955 is an example of a galaxy directed away from the cluster center, while the orbital motion of IC 711 around its cluster center is clearly visible due to its large size. The orientation of the radio tails of the rest of the sample head–tail radio galaxies seems to imply an orbital motion of the host galaxy around the cluster center rather than a radial infall. O’Dea et al. (1987) using a sample of 70 NAT radio sources, concluded that the head–tail sources are randomly oriented about the cluster center. Although our sample is statistically small, it seems that the random orientations of head–tail radio galaxies about the cluster center are consistent with the notion that the distribution of the orientations of these galaxies is isotropic (Rudnick & Owen 1976; Guindon 1978; Harris 1982; O’Dea et al. 1987).

As was already mentioned in Sections 4.1.2 and 4.1.7, two of the five tailed galaxies with both jets separately visible in our 610 MHz high resolution maps, the optical hosts are misplaced from the tip of the tails. Additionally, the intensity profiles of the jets in IC 711 are asymmetric (see Figure 11 and discussion in Sec. 5.4). The northern jet in it is seen to flare out at a larger projected distance from the core than the southern jet. This asymmetry in the jets in these three galaxies can occur if the jet axis is not aligned at 90° with the motion of the galaxy. However, this asymmetry may be due to projection effects (Reynolds 1980). Since it is known that there is no known correlation between the optical axes of the host galaxies and the jet axes of strong radio sources, there is no reason to expect a correlation between the jet axis and the motion of the galaxy in our sample of head–tail radio sources (Birkinshaw & Davies 1985; Battye & Browne 2009; Browne & Battye 2010). Hence the asymmetry in the jets is probably either due to projection effects or the ejection of the jet at acute angles with respect to the direction of motion of the host galaxy through the ICM.

Four out of five head–tail radio galaxies show both jets distinctly visible: namely, PKS B0053–016, PKS B0053–015, GB6 B0335+0955 and IC 711. They also show the presence of the multiple bends and wiggles, which are likely due to the precessing radio jets. Icke (1981) noticed similar features in the tail of 3C 129 and fitted precession models to the tail. O’Dea & Owen (1987) listed three possibilities for explaining the wiggles that were seen in NGC 1265: (1) precession, (2) helical instabilities, and (iii) variations in the momentum flux that possibly caused these wiggles. Though they do not rule out precession and variations in the momentum flux completely, they prefer helical instabilities over the other two possibilities. PKS B0053–016 has a symmetric structure. Though the helical features are not completely symmetric in the other three galaxies, it is noticeable that every loop or wiggle in one jet has a counterpart in the other. The other asymmetries possibly arise from the above-mentioned effects, namely acute angles between the direction of motion and jet axis, projection effects, and differences in their environments. Although NGC 7385 does not show any helical structures at the length scales seen in the rest of the four sources, the low-resolution images of it (Figure 8) show bends toward the ends of the tails, and it is not possible to completely rule out the possibility that the origin of these bends is similar to the ones seen in the rest of the four sources. For example, if precession leads to these features, then a smaller precessional velocity than the advancing speed of the galaxy through the ICM (Bliton et al 1998), might explain these large-scale bends.

5.2. Spectral Structure

We list a few qualitative points on the overall source spectral structures, based on the images presented in Figures 1–10 above.

- (i) A comparison of 610 and 240/325 MHz maps shows that large variations of spectral index ($\Delta\alpha \simeq 2.2$) occur in the tails of all head–tail radio galaxies.
- (ii) On moving along the tail from the head (or optical host galaxy), the spectrum typically steepens toward the ends of the tails.
- (iii) In the region where flaring occurs, there is a net increase in the total luminosity along with the flattening. This suggests that the particles are re-accelerated in or near this region.
- (iv) A steady decline in spectral index along the tail is not always seen in some of the galaxies. However, in most of these cases, the equipartition magnetic field and the net luminosity at the position of the discrepancy continue to follow the declining trend. Hence these discontinuities in the general steepening trends may be due to some turbulence that is present in the cluster environment, which leads to redistribution of the the energies of the electron population. It is possible that this turbulence is caused by the galactic wakes of the nearby galaxies (Jones & Owen 1979), by their gravitational influence.

- (v) The radiative age estimates are consistent with the hypothesis that the radio plasma ages due to synchrotron cooling as it moves away from the head of the radio galaxy, and the radio plasma at the farthest end is the oldest.
- (vi) The equipartition magnetic field and also the pressure in the farther end of the tail is lower by ~ 4 as compared to the region close to the core, which is similar to the result for 3C 129 (Lal & Rao 2004). There is a clear decrease in the spectral index and in the magnetic field values as one moves away from the core.
- (vii) In several galaxies, there is a jump in the steepening of the spectrum, such as in IC 711, where the jump in spectral index toward the end is quite significant. Similar complexities are also seen in IC 310, NGC 7385, NGC 1265 and GB6 B0335+0955. Such spectral index jumps were noted earlier by Wilson & Vallee (1977) as well, and this suggests reacceleration of electron population (Jaffe & Perola 1973; Lal & Rao 2004) in these regions due to shocks or turbulence in the cluster environment.
It is interesting to note the presence of IC 708, another massive head–tail radio galaxy close to this region showing a jump in spectral index. It is possible that this region of IC 711 showing a jump in spectral index is also under the gravitational influence of IC 708 (Figure 10). The interaction with nearby galaxies is also seen in GB6 B0335+0955. Hence the turbulence in the ICM induced by the random motions of galaxies passing close by could lead to the reacceleration of the particles in the tail.
- (viii) The energy of synchrotron-emitting electrons is redistributed in regions showing discontinuities in the spectra, i.e., the lower-energy electrons are energized to higher energies and hence the spectral index flattens. Furthermore, the total energy in these particles is conserved; in other words, since the flux density is seen to be reduced compared to the neighboring regions, there is no source of a fresh injection of electrons.

5.3. Dynamical age

The head–tail radio structure is strongly suggestive of the following scenario: the radio galaxy, in its orbital motion in the cluster, moves rapidly through the ICM; its radio components are slowed down by the ICM and lag behind the radio galaxy; and the farthest part of the radio source lags behind the radio galaxy. If this picture is correct, the velocity of the radio galaxy through the ICM and the radio properties of the head–tail sources give information on the time of ejection of relativistic particles by the galaxy and on the density of the ICM. Therefore, from the difference in cluster redshift and the galaxy redshift, the line-of-sight velocity of the galaxies was estimated. Further, assuming equal velocities along all three axes, the velocity in the plane of the sky would be on average $\sqrt{2}$ times the line-of-sight velocity. This and the projected length of the tails, which is used as a proxy for the distance traveled by the host galaxy, were

used in determining the dynamical ages of the head–tail radio galaxies.

TABLE 3
DYNAMICAL AGE ESTIMATES OF OUR SAMPLE SOURCES.

| Object | Velocity (km s ⁻¹) | size (l) (kpc) | age (Myr) |
|---------------|-----------------------------------|-----------------------|--------------|
| PKS B0053–016 | 785.1 | 5.3 238.9 | 295 |
| PKS B0053–015 | 3105.7 | 7.2 330.7 | 105 |
| IC 310 | 540.0 | 7.5 165.3 | 300 |
| NGC 1265 | 3760.5 | 10.0 220.4 | 55 |
| GB6 B0335+096 | 961.3 | 8.2 358.9 | 365 |
| IC 711 | 552.9 | 17.8 720.6 | 1275 |
| NGC 7385 | 428.2 | 14.3 442.3 | 1010 |

Table 3 presents these dynamical age estimates for our sample head–tail radio sources. Note that any head–tail radio galaxies which are nearly aligned along the line of sight may not be recognized as head–tail sources. These head–tail radio galaxies have relatively large velocities with respect to the ICM because of their motion along the line of sight.

A spectral aging analysis was done for the head–tail galaxies in Perseus cluster by Sijbring & de Bruyn (1998). The spectral age of NGC 1265 from their analysis and our dynamical ages are within the same order of magnitude. But the dynamical ages of IC 711 and NGC 7385 are about an order of magnitude higher, and that of NGC 1265 is an order of magnitude lower than their spectral or the radiative ages, whereas for the rest of the sample sources, the spectral ages and the dynamical ages are of the same order. This could mean that the direction of motion of NGC 1265 is not aligned to our line-of-sight whereas the direction of motion of IC 711 and NGC 7385 are aligned toward our line of sight. Given that the sample consists of large known head–tail radio galaxies, it is highly probable that the plane of the sky velocity is higher than what is assumed in most cases. Hence it is likely that the dynamical ages, presented in Table. 3 are an underestimation for NGC 1265 and an overestimation for IC 711 and NGC 7385. The dynamical ages of all of the galaxies in our sample are $(0.6\text{--}12.8) \times 10^8$ yr, with the median being 3.0×10^8 yr, are a factor of 1–20 more than the radiative age estimates of $(0.4\text{--}0.6) \times 10^8$ yr, with the median being $\sim 0.5 \times 10^8$ yr for our head–tail sample sources.

5.4. Roles of interstellar and intracluster media

Gunn & Gott (1972) proposed that the infall of galaxies onto cluster potential during the early phases leads to ram pressure stripping of the ISM in these galaxies. Hence, elliptical galaxies, especially those in clusters, are poor in gas content. However, Jones & Owen (1979) show that elliptical galaxies moving through a cluster can still retain a significant amount of ISM within ~ 10 kpc, called as the influence of the ISM. Since in some radio sources the scales of bending usually seen in head–tail radio sources are similar to the size of influence of the ISM, it suggests that the ISM may be important in the formation of head–tail radio sources. Qualitatively, when a galaxy is moving at a transonic speed through the ICM, a bow shock is expected to develop at the leading edge of the galaxy, assuming that some amount of ISM is retained

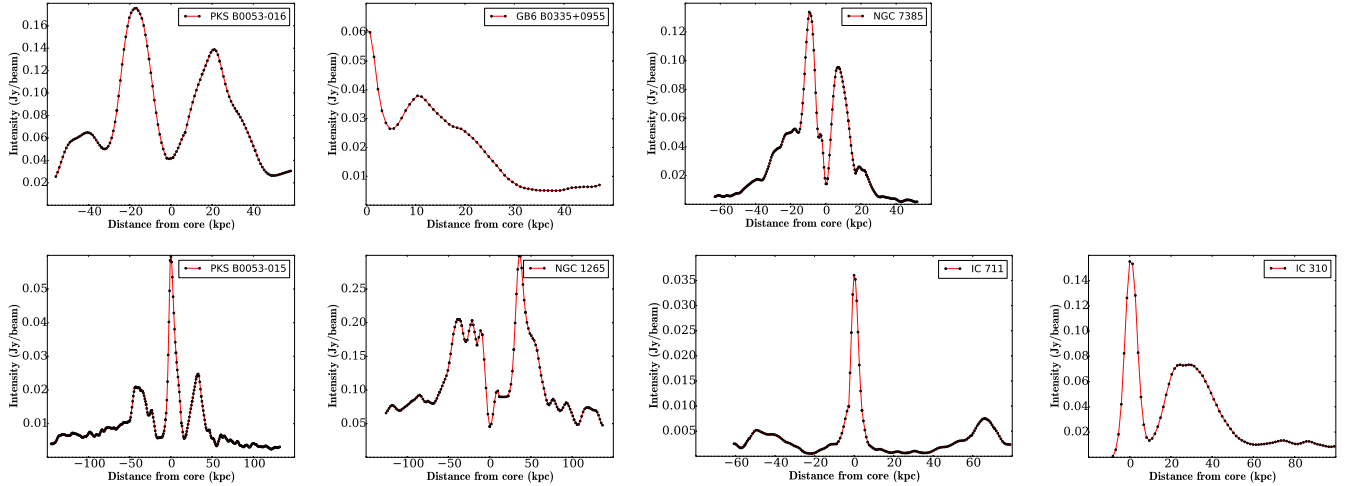


FIG. 11.— The spatial profile of radio intensity in the inner parts at 610 MHz as a function of distance from radio core along the ridge line. The profiles for all our sample sources are ordered as, clockwise from top left, PKS 0053–016, GB6 B0335+0955, NGC 7385, IC 310, IC 711, NGC 1265 and PKS 0053–015, same as Fig 1. The radio intensity profiles are shown along both radio jets, except for GB6 B0335+0955 and IC 310. The position of the peak radio intensity away from the radio core along the ridge line marks the location of the flaring.

within the galaxy (Jones & Owen 1979). Consequently, a turbulent galactic wake would be formed behind the galaxy, and that the flaring seen in head–tail galaxies occurs when the radio jets are re-accelerated as a result of the turbulence in the galactic wake (Jones & Owen 1979). Hence, in this context, below we discuss if the head–tail radio galaxies in general show similar deceleration phenomena and at what size scales.

Head–tail radio sources are considered to form a subset of the FRI type sources and all FRI sources, have a region with a sudden increase in brightness close to the core. The initially relativistic jet is thought to be decelerated to sub-relativistic speeds at the flaring point, which is due to entrainment of the surrounding material or by injection of stellar ejecta (Bicknell 1994; Komissarov 1994; Bicknell 1995). The flux ratio of the jet to its counterjet along the distance from the core suggests that an initially relativistic jet with velocity $\sim 0.6c$ decelerates to sub-relativistic speeds, $\sim 0.1c$ within ~ 5 kpc (Parma et al. 1994). Figure 11 shows plots of radio intensity in the inner parts at 610 MHz as a function of distance from the core along the ridge line for our sample of head–tail radio sources. Although the flaring is not always very smooth in every galaxy, the projected lengths, on an average, are always $\gtrsim 5$ kpc, whereas, according to Jones & Owen (1979), the location of flaring must depend on the size scale of the ISM, which depends on the ICM density (Gregorini & Bondi 1989), ram pressure and so on. The location of the maxima of the flaring varies from $\simeq 15$ kpc in NGC 7385 and GB6 B0335+0955 to $\gtrsim 60$ kpc in IC 711. In addition, there are some asymmetries at the location of the flare in several head–tail radio galaxies, such as in IC 711, which might be due to several reasons discussed in Section 5.1. These differences in the distances of the flaring in our sample sources could be attributed due to the difference in environments along with projection effects and ejection of the jet at acute angles with respect to the direction of motion of the host galaxy through the ICM. Additionally, an independent study of WATs O’Donoghue, Eilek & Owen (1993) found a range from

~ 15 to ~ 119 kpc for locations of the radio flaring. It is also possible that the distances at which flaring occurs in our sample of head–tail radio sources may appear small due to projection, and hence actual sizes of the flaring region may be larger. Nevertheless, it is clear that flaring can appear at locations as large as ~ 60 kpc, in our sample or ~ 119 kpc in O’Donoghue, Eilek & Owen (1993) sample sources, and it is unlikely that the ISM extends to such large values.

Instead, flaring at such large distances from the core are likely due to environmental disturbances, such as from the entrainment by hot ICM, consistent with Bicknell (1994), Komissarov (1994) and Bicknell (1995). Indeed, the ICM within merging clusters of galaxies is likely to be in a violent or turbulent dynamical state and may have significant effect on the evolution of cluster radio sources (Bliton et al 1998). The three-dimensional simulations of jets propagating in such ICMs show that a collimated radio jet encountering a surface brightness edge in a merging cluster environment disrupts and flares as a result of Kelvin–Helmholtz instabilities (Loken et al. 1995).

6. SUMMARY

We have presented the GMRT data for the seven large known head–tail radio galaxies. By examining the gross characteristics, several conclusions are drawn by examining the gross morphological structures, spectral structures, equipartition parameters, and kinematics of these head–tail radio galaxies.

1. The sample is composed of seven large head–tail galaxies in terms of their angular sizes. All these were found to be hosted by prominent and massive elliptical galaxies. Additionally, massive neighboring galaxies can distort a simple orbital motion trajectory of head–tail radio galaxies, as is seen in GB6 B0335+0955, IC 711 and NGC 7385.
2. Five sources in the sample show clear, distinguishable radio tails or jets seen in high-resolution images, two sources have their optical hosts away from

the tip of their radio emission tails. This suggests that there is no preferential orientation of the radio jet with respect to the direction of motion of the host galaxy.

3. Four of the five head–tail radio galaxies, namely, PKS B0053–016, PKS B0053–015, GB6 B0335+0955 and IC 711 with clear distinguishable radio tails/jets show the clear presence of the multiple bends and wiggles. The presence of these wiggles is possibly due to the precession of the jet.
4. In almost all of the sources in the sample, we see a flaring in the intensity of the jet close to the core; the radio jet spreads out and disappears into lower surface brightness radio emission. The spectral index of the radio jet is flatter near the core. It begins to flare as it encounters a surface brightness edge, and the spectral index begins to steepen immediately after the location of flaring. The spectral index is the steepest in regions with lower surface brightness, that is, at the farthest end of tails. Furthermore, the bulk kinetic energy of the jet is probably being converted into the internal energy, which explains the possible increase in the total radio emission along with a relatively flat radio spectrum.
5. Since projection effects result in the classification of many of the WAT sources as NAT sources, these NAT sources are our best bet to look directly into a spatially extended radio source nucleus according to unification theory, as evidenced in the case of IC 310.
6. By examining the gross spectral structure, we find steepening of the radio spectrum in all head–tail radio galaxies, and we do not see evidence for a region with a constant spectral index (see Section 1). We believe this is due to coarser sampling of regions, and within error bars, the results are consistent.

7. The equipartition magnetic field is also seen to fall as distance from the head along the tail increases. But there are regions where the magnetic field does not show a smooth decline, whereas the spectral index shows a smooth decline. Since we assumed cylindrical symmetry, the equipartition magnetic field is proportional to $(L/V)^{2/7}$ and given that the radio tails might overlap at least in projection, we might be underestimating the volume at such regions, which in turn leads to overestimation of the equipartition magnetic field.

In a subsequent paper, we will discuss the radio intensity and surface brightness gradients and the X-ray properties of these head–tail radio sources. Furthermore, since the X-ray data are indicative of an ICM, there may be a contact surface brightness edge just before the flaring of the radio jet, as suggested by [Loken et al. \(1995\)](#). Therefore, we will also investigate the morphological properties of a propagating jet, say as it crosses its ISM into an ICM. Also, a comparison of the particle density inside the tails with respect to the external gas density via thermal bremsstrahlung would be investigated in order to probe the conditions applicable for buoyancy or falling in this head–tail radio galaxies sample.

ACKNOWLEDGMENTS

We thank the anonymous referee for his or her prompt review of this manuscript and for comments that led to the improvement of this paper. We also thank D. A. Green, P. Kharb and S. N. Murthy, and S. Vaddi for discussions and several useful comments. We thank the staff of the GMRT who have made these observations possible. The GMRT is run by the National Center for Radio Astrophysics of the Tata Institute of Fundamental Research. This research has made use of the NASA/IPAC Extragalactic Database (NED), which is operated by the Jet Propulsion Laboratory, California Institute of Technology, under contract with the NASA, and NASA’s Astrophysics Data System.

REFERENCES

- Aleksić, J., Antonelli, L. A., Antoranz, P., et al. 2014, *A&A*, 563A, 91
- Baan, W. A. & McKee, M. R. 1985, *A&A*, 143, 136
- Balsara, D. S. & Norman, M. L. 1992, *ApJ*, 393, 631
- Battye, R. A., & Browne, I. W. A. 2009, *MNRAS*, 399, 1888
- Browne, I. W. A., & Battye, R. A. 2010, in *ASP Conf. Ser.* 427, *Accretion and Ejection in AGN: a Global View*, ed L. Maraschi et al. (San Francisco, CA: ASP), 365
- Begelman, M. C., Rees, M. C. & Rees, M. J. 1979, *Nature*, 279, 770
- Bicknell, G. V. 1994, *ApJ*, 422, 542
- Bicknell, G. V. 1995, *ApJS*, 101, 29
- Birkinshaw, M., & Davies, R. L. 1985, *ApJ*, 291, 32
- Blanton, E. L., Gregg, M. D., Helfand, D. J., Becker, R. H., White, R. L. 2003, *AJ*, 125, 1635
- Blanton, E. L., Gregg, M. D., Helfand, D. J., Becker, R. H., & White, R. L. 2000, *ApJ*, 531, 118
- Blanton, E. L., Gregg, M. D., Helfand, D. J., Becker, R. H., & Leighly, K. M. 2001, *AJ*, 121, 2915
- Bliton, M., Rizza, E., Burns, J. O., Owen, F. N., & Ledlow, M. J. 1998, *MNRAS*, 301, 609
- Burbidge, G. R. 1956, *ApJ*, 124, 416
- Burns, J. O. 1981, *MNRAS*, 195, 523
- Burns, J. O., Eilek, J. A., & Owen, F. N. 1982, *IAU Symposium* 97, *Extragalactic Radio Sources*, ed. D. Heeschen and C. Wade (Dordrecht: Reidel), p.45
- Edge, A. C. & Ottgering, H. 1995, *MNRAS*, 277, 1580
- Eilek, J. A., Burns, J. O., O’Dea, C. P., & Owen, F. N. 1984, *ApJ*, 278, 37
- Fanaroff, B. L. & Riley, J. M. 1974, *MNRAS*, 167P, 31
- Feretti, L., Giovannini, G., Klein, U., Mack, K.-H., Sijbring, L. G., Zech, G. 1998, *A&A*, 331, 475
- Feretti, L., Dallacasa, D., Govoni, F., et al. 1999, *A&A*, 344, 472
- Gan, Z., Li, H., Li, S., & Yuan, F. 2017, *ApJ*, 839, 14
- Gregorini, L. & Bondi, M. 1989, *A&A*, 225, 333
- Guindon, B. 1978, *MNRAS*, 183, 195G
- Gunn, J. E. & Gott, J. R. 1972, *ApJ*, 176, 1
- Hardee, P. E., Eilek, J. A. & Owen, F. N. 1980, *ApJ*, 242, 502H
- Harris, D. E. 1982, *IAUS*, 97, 77H
- Icke, V. 1981, *ApJL*, 246, L65
- Jaegers, W. J. 1987, *A&AS*, 71, 603
- Jaffe W. J. & Perola, G. C. 1973, *A&A*, 26, 423
- Jones, T. W. & Owen, F. N. 1979, *ApJ*, 234, 818
- Jones, T. W., Nolting, C., O’Neill, B. J., & Mendygral, P. J. 2017, *Physics of Plasmas*, 24, 041402
- Kharb, P., Lister, M. L. & Cooper, N. J. 2010, *ApJ*, 710, 764

- Komissarov, S. S. 1994, *MNRAS*, 269, 394
- Lal, D. V. & Rao, A. P. 2004, *A&A*, 420, 491
- Lal, D. V. & Rao, A. P. in *From Clark Lake to the Long Wavelength Array: Bill Erickson's Radio Science*, edited by N. Kassim, M. Perez, W. Junor & P. Henning 2005, *Astronomical Society of the Pacific Conf. Ser.*, 345, 289
- Lal, D. V. & Rao, A. P. 2007, *MNRAS*, 374, 1085
- Lal, D. V., Hardcastle, M. J. & Kraft, R. P. 2008, *MNRAS*, 390, 1105
- Loken, C., Roettiger, K.; Burns, J. O., Norman, M. 1995, *ApJ*, 445, 80
- Mack, K.-H., Feretti, L., Giovannini, G., & Klein, U. 1993, *A&A*, 280, 63
- Mariotti, M. 2010, *ATel*, 2510, 1M
- Miley, G. K., Perola, G. C., van der Kruit, P. C. & van der Laan, H. 1972, *Nature*, 237, 269
- Miley, G. K. 1973 *A&A*, 26, 413
- Miley, G. K. 1980 *ARAA*, 18, 165
- Moffet, A. T. in *Galaxies and the Universe*, edited by A. Sandage, M. Sandage, & J. Kristian 1975 *Stars and Stellar Systems*, Univ. of Chicago Press, 9, 211
- Owen, F. N. & Ledlow, M. J. 1997, *ApJS*, 108, 41
- O'Dea, C. P. & Owen, F. N. 1985, *AJ*, 90, 927
- O'Dea, C. P. 1985, *ApJ*, 295, 80
- O'Dea, C. P. & Owen, F. N. 1986, *ApJ*, 301, 841
- O'Dea, C. P., & Owen, F. N. 1987, *ApJ*, 316, 95
- O'Dea, C. P., Sarazin, C. L. & Owen, F. N. 1987, *ApJ*, 316, 1130
- O'Donoghue, A. A., Eilek, J. A. & Owen, F. N. 1993, *ApJ*, 408, 428
- Paterno-Mahler, R., Blanton, E. L., Brodwin, M., et al. 2017, *ApJ*, 844, 78
- Parma, P., de Ruiter, H. R., Fanti, R., & Laing, R. 1994, in *ASP Conf. Ser. 100, The Physics of Active Galaxies*, ed G. V. Bicknell, M. A. Dopita, & P. J. Quinn (San Francisco: ASP), 241
- Pacholczyk, A. G. & Scott, J. S. 1976, *ApJ*, 203, 313
- Prasad, J. & Chengalur, J. N. 2012, *Ex. A.*, 33, 157
- Pfrommer, C.; Jones, T. W. 2011, *ApJ*, 730, 22
- Rawes, J., Worrall, D. M. & Birkinshaw, M. 2015, *MNRAS*, 452, 3064R
- Reynolds, J. E. 1980, *Proceedings of the Astronomical Society of Australia*, 4, 74
- Rudnick, L. & Owen, F. N., 1976, *ApJ*, 203L, 107R
- Ryle, M. & Windram, M. D. 1968, *MNRAS*, 138, 1
- Sarazin, C. L., Baum, S. A. & O'Dea, C. P. 1995, *ApJ*, 451, 125S
- Schilizzi, R. T., & Ekers, R. D. 1975, *A&A*, 40, 221
- Sijbring, D. & de Bruyn, A. G. 1998, *A&A*, 331, 901
- Spergel, D.N., Bean, R., Doré, O., et al. 2007, *ApJS*, 170, 377
- Srivastava, S. & Singal, A. K. 2016 ,
- Vallee, J. P. & Roger, R. S. 1987, *AJ*, 94, 1V
- Vallee, J. P. 1988, *Ap&SS*, 149, 225V
- Vallee, J. P. & Strom, R. G. 1988, *AJ* 95 1360V
- Williams, A. G. & Gull, S. F. 1984, *Nature*, 310, 33
- Wilson, A. S. & Vallee, J. P. 1977, *A&A* 58 79
- Wing, J. D., & Blanton, E. L. 2011, *AJ*, 141, 88